

1 **Ultramafic-hosted Ni-Cu-Co-(As) mineralization from an ancient oceanic transform fault zone in the**  
2 **Troodos ophiolite, Cyprus: an analogue for ultramafic seafloor massive sulfide mineralization?**

3 <sup>1,2\*</sup>Andrew J. Martin, <sup>3</sup>Christopher J. MacLeod, <sup>4</sup>Katie A. McFall, <sup>3</sup>Iain McDonald, <sup>1</sup>John W. Jamieson and  
4 <sup>3</sup>Sophie Cox

5 <sup>1</sup> Department of Earth Sciences, Memorial University of Newfoundland, Canada

6 <sup>2</sup> Department of Geoscience, University of Nevada, Las Vegas, USA

7 <sup>3</sup> School of Earth and Environmental Sciences, Cardiff University, UK

8 <sup>4</sup> Earth Sciences, University College London, UK

9 \*Corresponding author: Andrew J. Martin (Andrew.martin@unlv.edu)

10 **Abstract**

11 Accumulations of sulfide minerals that are enriched in Ni-Cu-Co-(As) occur as seafloor massive sulfide  
12 (SMS) deposits associated with ultramafic lithologies on the seafloor and in ophiolite terranes as  
13 Outokumpu-type mineralization. In this study we focus on similar mineralization at Lakxia tou Mavrou in  
14 the Limassol Forest Complex of Cyprus, which represents the on-land exposure of an oceanic transform  
15 fault zone preserved within the Troodos ophiolite. Mineralization here consists of massive lenses of  
16 pyrrhotite associated with veins of isocubanite, chalcopyrite, Co-pentlandite and chrome spinel hosted in  
17 serpentinized mantle peridotite. We re-examine the field context of mineral occurrences and use *in situ*  
18 mineral chemistry, element mapping and sulfur isotope ratios ( $\delta^{34}\text{S}$ ) to constrain metal sources and provide  
19 an updated paragenetic model for Lakxia tou Mavrou. Highly variable S/Se ratios (304 to 108,571), a  
20 depletion in platinum group elements relative to mantle values and an average  $\delta^{34}\text{S}$  value of  $-3.7\pm 2.4\%$  ( $1\sigma$ ,  
21  $n=17$ ) in sulfide minerals support a hybrid hydrothermal and magmatic origin for the mineralization. Metals  
22 at Lakxia tou Mavrou were sourced from both the serpentinization of peridotites and from cross-cutting  
23 intrusions, with later intrusions into the already serpentinized mantle lithosphere host providing a heat

24 source to drive prolonged hydrothermal circulation. The re-examination of the field context of  
25 mineralization shows that the Ni-Cu-Co-(As) mineralization at Lakxia tou Mavrou originally formed as a  
26 consequence of the fault-guided intrusion of hot primitive magma bodies into serpentinized shallow mantle  
27 lithosphere in the active domain of an ocean-floor transform fault zone. The mineralization was  
28 subsequently partially disrupted by structures related to emplacement of the Troodos ophiolite. We show  
29 that the relationship between serpentinization, magmatism and hydrothermal circulation at Lakxia tou  
30 Mavrou can be used to understand the formation of ultramafic-hosted SMS deposits in transform fault and  
31 other ultramafic-dominated slow- and ultraslow-spreading mid-ocean ridge settings.

## 32 Introduction

33 Serpentinization of peridotites at and below the seafloor occurs during seawater circulation where primary  
34 igneous olivine and pyroxene are hydrated to form secondary minerals such as chrysotile, lizardite,  
35 antigorite and magnetite (Alt and Shanks, 2003; Mével, 2003). The destruction of olivine and pyroxene  
36 during serpentinization releases large quantities of Ni, Co and Fe that are hosted within these minerals.  
37 Simple cooling and serpentinization of peridotite is normally thought insufficient in itself to generate  
38 significant metal concentrations (Petersen et al. 2009; Allen and Seyfried, 2003). To form sulfide  
39 mineralization an additional heat source is required to drive high-temperature (~350°C) fluid circulation  
40 and to transport Ni, Co and Fe in hydrothermal fluids to the seafloor, potentially to form seafloor massive  
41 sulfide (SMS) deposits (Fouquet et al., 2010). Seafloor massive sulfide deposits form during the interaction  
42 of seawater with underlying magma chambers in oceanic crust where high-temperature (>350°C) seawater-  
43 derived hydrothermal fluid leaches metals from the underlying crust. The metals are then transported in the  
44 hydrothermal fluid and exhaled on the seafloor to form hydrothermal precipitates (e.g., Hannington et al.  
45 2005). The study of SMS deposits is of particular interest as they represent actively-forming analogues to  
46 ancient volcanogenic massive sulfide (VMS) deposits that are preserved in ophiolite terranes (e.g., Peltonen

47 et al. 2008). However, the relationship between igneous intrusions, serpentinization and SMS deposit  
48 formation remains poorly characterized in both ancient and active deposits.

49 Environments in which areas of serpentinized mantle lithosphere are exposed at the Earth's surface are now  
50 known to be far more commonplace in the ocean basins than previously thought (Mével, 2003). Mantle-  
51 derived ultramafic lithologies, that are variably serpentinized, represent ~20-25% of the seafloor at slow-  
52 to ultra-slow spreading mid-ocean ridges (<40 mm a year), representing ~14,660 km of the present day  
53 ridge system (Cannat et al., 2010), principally along large-offset extensional detachment faults (e.g.,  
54 Cannat, 1993; Cann et al., 1997). Ocean-floor serpentinization of the mantle appears also to be widespread  
55 at oceanic transform plate boundaries (e.g., Francis, 1981), where oceanic crust is thin, fractured and  
56 permeable. Increased permeability facilitates seawater circulation deep into the mantle lithosphere and  
57 promotes the serpentinization of lithospheric mantle peridotite (Francis, 1981; McCaig et al., 2007). Mafic  
58 igneous intrusions into mantle lithosphere have been documented in both detachment fault footwalls (e.g.,  
59 15°45'N on the Mid-Atlantic Ridge: MacLeod et al., 2002; Escartin et al., 2003, Atlantis Massif: Ildefonse  
60 et al., 2007) and in oceanic transform fault zones (e.g., Siqueiros transform zone: Fornari et al., 1989;  
61 Garrett transform zone: Hekinian et al., 1992). Spatially related SMS deposits occur both at or away from  
62 the spreading axis in ultramafic seafloor (e.g., Rona et al., 1987; Krasnov et al., 1995; Cherkashev et al.,  
63 2013; Petersen et al., 2009). For example, the Semenov-2 hydrothermal field at 13°30' N on the Mid-  
64 Atlantic Ridge forms ~5.5 km away from the spreading ridge axis (Escartin et al., 2017). However, no  
65 equivalent such deposits have been reported from oceanic transform faults, though there is potential for  
66 them to form in this tectonic environment, as the crust is highly permeable due to faulting and syn-tectonic  
67 magmatic intrusions can occur (Francis, 1981; Fornari et al., 1989; Hekinian et al., 1992).

68 Because of the technical and logistical challenges, little is known of the controls on sulfide mineralization  
69 in serpentinite-hosted seafloor environments. Potential insight may however be derived from the study of  
70 ophiolites. Numerous occurrences of Ni-Cu-Co-(As) mineralization are associated with ultramafic host  
71 rocks in ophiolite complexes. These are termed "Outokumpu-type" sulfide deposits (e.g., Bou Azzer,

72 Morocco), and could represent ancient analogues to ultramafic-hosted SMS deposits actively-forming along  
73 slow- and ultraslow-spreading mid-ocean ridges. However, linking the formation of Outokumpu-type  
74 deposits to seafloor processes remains speculative (e.g., Coltat et al., 2021). Examples of ultramafic-hosted  
75 occurrences on the modern seafloor include Ashadze, Logatchev, Semenov, Rainbow, Longqi-1, Kairei and  
76 Von Damm vent fields (Leblanc and Billaud, 1982; Fouquet et al., 1997; Peltonen et al., 2008; Petersen et  
77 al., 2009; Fouquet et al., 2010; Connelly et al., 2012; Melekestseva et al., 2014, 2020; Wang et al., 2018;  
78 Tao et al., 2020; Patten et al., 2022). These sulfide deposits are enriched in Ni and Co relative to deposits  
79 hosted in mafic environments (Hannington et al., 2005). By comparison, Outokumpu-type deposits contain  
80 higher contents of Ni, Cu and Co and have a higher tonnage relative to known ultramafic-hosted SMS  
81 deposits. For example, at Outokumpu, the ore reserve was 28.5 Mt at 3.8 wt.% Cu, 0.24 wt.% Co and 0.12%  
82 Ni (Parkkinen, 1997). With the exception of the Semenov hydrothermal field (13°30' N, MAR) that has an  
83 estimated tonnage of 40 Mt, most other deposits are smaller, for example Ashadze at 5.2 Mt or Logachev  
84 at 1.9 Mt (Cherkashev et al., 2013). In ancient terranes, most Outokumpu-type deposits occur within highly  
85 metamorphosed regions (up to amphibole facies), in which primary mineral textures and geochemical  
86 signatures have been overprinted or modified during metamorphism (e.g., Bou Azzer, Morocco or  
87 Kylylahti, Finland; Leblanc and Billaud, 1982; Peltonen et al., 2008). Metamorphic upgrading of the  
88 deposits, where metals are remobilized and concentrated, is proposed to be an important process in  
89 achieving economic metal grades (Peltonen et al., 2008).

90 In this study we examine an occurrence of Ni-Cu-Co-(As) sulfide mineralization in serpentinized peridotite  
91 within a late Cretaceous oceanic transform fault preserved in the Troodos ophiolite of Cyprus. The  
92 mineralization, at the Lakxia tou Mavrou occurrence, may have partially formed by hydrothermal processes  
93 analogous to modern ultramafic-hosted SMS deposits. We investigate the geological setting of the  
94 mineralization and evaluate its comparability to similar hydrothermally active ultramafic settings on the  
95 modern ocean-floor and compare these to Outokumpu-type deposits. We find that sulfur isotope ratios,  
96 sample mineralogy, and elemental compositions are different between Lakxia tou Mavrou and a typical

97 Troodos mafic-hosted VMS deposit, and that these differences can be related to the specific tectonic setting  
98 of Lakxia tou Mavrou. Our findings confirm that Lakxia tou Mavrou did not form at the seafloor, but rather  
99 below the seafloor from hydrothermal processes generated by interactions of magma intrusions into  
100 already-serpentinized peridotite, forming a hybrid between SMS and Outokumpu-type deposits. We  
101 highlight the potential for replacement-type sulfide mineralization to form in ultramafic rocks deep below  
102 the seafloor and in associated ophiolite terranes.

## 103 Geological Background

### 104 *The Troodos ophiolite*

105 The Troodos ophiolite of Cyprus is a fragment of Cretaceous oceanic lithosphere (~92 Ma; Mukasa and  
106 Ludden, 1987) formed by seafloor spreading in a supra-subduction zone environment (Miyashiro, 1973;  
107 Pearce, 1975; Gass, 1980). The Troodos Massif preserves a complete Penrose stratigraphy: mantle  
108 peridotites are overlain by a continuous 4-5 km-thick oceanic crust comprising ultramafic and mafic  
109 plutonic rocks, a regionally extensive sheeted dyke complex and an extrusive lava sequence of arc tholeiite  
110 to boninite composition (e.g., Gass, 1968; Moores et al., 1971; Pearce and Robinson, 2010). Troodos was  
111 then later uplifted and exhumed in the Miocene (Robertson, 1977).

### 112 *Arakapas Fault Belt and Limassol Forest Complex: the “Southern Troodos Transform* 113 *Fault Zone”*

114 The southern margin of the Troodos massif, the Arakapas Fault Belt and Limassol Forest Complex region,  
115 is characterized by more complex geological relationships than in the remainder of the ophiolite (Fig. 1A  
116 and B). The Arakapas Fault Belt and Limassol Forest Complex are generally accepted as forming part of a  
117  $\geq 5$  km wide E-W trending syn-accretionary seafloor fault zone that represents an oceanic transform fault  
118 (Moores et al., 1971; Simonian and Gass, 1978) referred to as the Southern Troodos Transform Fault Zone  
119 (STTFZ). A small sliver of Anti-Troodos crust from the opposite plate is preserved in the southeastern

120 Limassol Forest Complex (MacLeod, 1990; Gass et al., 1994), and a fossil ridge-transform intersection lies  
121 to the present-day southwest of Mount Olympus (MacLeod et al., 1990).

122 The Arakapas Fault Belt forms the northern margin of the STTFZ (Fig. 1B), at paleo-seafloor level, prior  
123 to uplift and exhumation, and consists of an E-W trending zone of sheeted dykes and lavas cut by numerous  
124 braided fault strands of intense brittle strike-slip deformation, forming a laterally continuous zone of  
125 faulting extending for over 30 km E-W along strike (Simonian, 1975; Simonian and Gass, 1978; MacLeod  
126 and Murton, 1993; Fagereng and MacLeod, 2019).

127 The Limassol Forest Complex is characterized by deep erosional levels (~3-4 km; Murton et al., 1986a)  
128 geometrically complex dismembered, rotated and intercalated fault blocks from all stratigraphic levels,  
129 including extensive areas of serpentized mantle peridotite (Fig. 1B). Across the western Limassol Forest  
130 Complex extensive deformation is manifested as high-strain, dextral strike-slip serpentinite shear zones up  
131 to hundreds of meters wide and traceable along strike for a few tens of km (Murton 1986a; MacLeod and  
132 Murton, 1993, 1995; Fagereng and MacLeod, 2019; Cox et al., 2021). These shear zones cut, but are  
133 themselves also cross-cut, by extensive syn-tectonic ultramafic and mafic magmatic intrusions of boninitic  
134 composition. These “Transform Sequence” intrusions take the form of plutons hundreds of meters to several  
135 km wide, accompanied by voluminous swarms of dykes (locally sheeted, and forming up to 22% of the  
136 local area: Murton, 1986a), that intrude already-serpentized host mantle lithosphere, earlier “Axis  
137 Sequence” crustal blocks and shear zones (Murton 1986a, b; MacLeod and Murton, 1993, 1995; Gass et  
138 al., 1994). These relationships indicate transtension and magma focusing into a locally “leaky” active  
139 ocean-floor transform plate boundary (Murton 1986a; Gass et al., 1994). Significantly, the pervasive  
140 serpentization of >3 km of the lithospheric mantle in the Limassol Forest Complex occurred prior to and  
141 during transform-related deformation and intra-transform magmatic intrusion and indicates deep, wholesale  
142 penetration of seawater into the active domain of the transform (Murton, 1986a, MacLeod and Murton,  
143 1993, 1995; Cox et al., 2021).

144 *Lakxia tou Mavrou*

145 The Ni-Cu-Co-(As) mineralized zone at Lakxia tou Mavrou is located ~1.5 km south of the village of  
146 Dhierona (Fig. 1B). It lies within sheared, serpentinitized mantle rocks of the western Limassol Forest  
147 Complex, near a faulted boundary with the sheeted dyke complex (Fig. 1B and C), and therefore within the  
148 original ocean-floor transform-tectonized domain and at relatively deep levels (~3-4 km) beneath the  
149 seafloor of the original transform fault valley. Its local geological setting is complex, due to multiple  
150 generations of seafloor and uplift related deformation but decipherable in the broader context of the  
151 tectonics of the Limassol Forest Complex (Gass et al., 1994).

152 On the 1:25,000 scale maps of Gass et al. (1994), Lakxia tou Mavrou is located within a ~300 m wide zone  
153 of E-W trending sheared serpentinite that, to the west, continues for several km (Fig. 1B and C).  
154 Serpentinitized mantle peridotite forms the southern margin of this shear zone. To the north, sheeted dykes  
155 are indicated as forming the northern margin for the first kilometer west of Lakxia tou Mavrou and then  
156 serpentinitized mantle peridotite farther to the west (Fig. 1C). To the east of Lakxia tou Mavrou, however,  
157 the serpentinite shear zone is marked as turning towards the ESE, and effectively merging with a broad,  
158 compound zone of WNW-ESE faulting termed the “Pevkos Fault” that can be traced ~11 km further to the  
159 ESE (Fig. 1C; MacLeod, 1990).

160 The Pevkos Fault has a protracted history, originally having a down-to-the-SSE sense of movement that  
161 cuts an earlier regionally extensive sub-horizontal detachment fault, the Akapnou Forest Décollement  
162 (AFD) that separates plutonic rocks and serpentinitized peridotite (MacLeod, 1988, 1990; Gass et al., 1994;  
163 Fig. 1C). To the SE, the Pevkos Fault separates plutonic rocks from Anti-Troodos lavas, with  $\geq 3$  km total  
164 displacement (total crustal thickness of ~4km for Anti-Troodos: MacLeod, 1988). The Pevkos Fault is  
165 demonstrably younger than the transform-related E-W structures (Fig. 1C). From our own field  
166 investigations, we have ascertained that rather than merging in the vicinity of Lakxia tou Mavrou, WNW-  
167 trending faulting related to the Pevkos Fault zone instead cuts across the earlier E-W dextral strike-slip

168 shear zone. This is evident in local-scale geological maps of Lakxia tou Mavrou, in which broadly WNW  
169 to NW-striking fault or shear zones are shown to cut the area, including pre-existing sheared serpentinite  
170 (Fig. 1D: Panayiotou, 1980; BMG, 2013). Moreover, sheeted dykes do not form the northern margin to the  
171 transform-related E-W serpentinite shear zone to the east of Lakxia tou Mavrou (Fig. 1C). Instead, the  
172 contact between the dykes and serpentinite represents a westerly continuation of the same Akapnou Forest  
173 Décollement (Fig. 1C; MacLeod, 1990; Gass et al., 1994).

174 Mineralization at Lakxia tou Mavrou is preserved in the E-W serpentinite shear zone, where it is spatially  
175 associated with Transform Sequence intrusions. Greenschist facies, slightly rodingitized, hydrothermally  
176 altered boninitic dykes have been intruded into serpentinite, chilled and then sheared/boudinaged into cm  
177 to m-sized phacoidal blocks within the phyllonitic serpentinite shear zone (Fig. 2A). The dykes are also  
178 notable for containing 1-2% of 2-3 mm-diameter spherical sulfide blebs. The vertical E-W trending host  
179 serpentinite shear zone has dextral S-C shear sense indicators (Fig. 2B and C), with chrysotile forming the  
180 main serpentinite polymorph indicating that most deformation took place at temperatures in the range of  
181 200-300°C (Cox et al., 2021). Textures in core samples of the sulfide mineralization itself indicate ductility  
182 (Fig. 2D, E and F), but pyrrhotite and chalcopyrite, which dominate here, have been shown to deform in  
183 this fashion at temperatures as low as ~100°C and  $\leq$ ~200°C, respectively (Marshall and Gilligan, 1987  
184 Cook et al., 1993; LaFrance et al., 2020).

185 The mineralized zone is characterized by massive, veined, and disseminated sulfide mineralization with  
186 trace amounts (<1 wt.%) of arsenide minerals (Foose et al., 1985; Thalhammer et al., 1986). Pyrrhotite,  
187 chalcopyrite, isocubanite, and pentlandite form the main sulfide minerals with trace amounts (<1 wt.%) of  
188 cobaltite (CoAsS), maucherite (Ni<sub>11</sub>As<sub>8</sub>), and löllingite (FeAs<sub>2</sub>) (Panayiotou 1980). At the surface, a gossan  
189 of pyrrhotite and Fe-oxide outcrops and historic adits are accessible (Fig. 1D). Drilling of Lakxia tou  
190 Mavrou in 2013 by Brazilian Metals Group (BMG) produced intersections of 4.3 m at 2.5% Cu and 4.2 m  
191 at 1.7% Cu, 1.18 g/t Au and 0.15% Co (BMG, 2015). The mineralized package dips steeply (>60°) to the  
192 north and varies in thickness from 20-40 m wide with gossan exposures traceable for ~1.5 km along strike



193 (BMG, 2015). The morphology of sulfide mineralization varies along strike and spatially across the  
194 serpentinite shear zone, with massive lenticular sulfide bodies and veins more common to the north, and  
195 disseminated sulfide mineralization more common to the ESE at a smaller sulfide occurrence called Pevkos  
196 (~5km; Fig 1B; Panayiotou, 1980). The Pevkos deposit was, however, even more heavily disrupted and  
197 modified by the later tectonic events referred to in the preceding section and its original paragenetic  
198 relationships are less clear. In addition to a high-degree of deformation, mineralization at Pevkos was  
199 inaccessible at the time of study and hence is not considered further in this study.

## 200 Methods

### 201 *Mineralogy*

202 Reflected light microscopy was undertaken on representative polished mounts ( $n=10$ ) prior to scanning  
203 electron microscope (SEM) analysis. Element mapping was performed on a Zeiss Sigma HD Automated  
204 Scanning Electron Microscope (ASEM) equipped with two Oxford Instruments X-Max<sup>N</sup> 150 mm large area  
205 Silicon Drift Detectors at Cardiff University, UK. The SEM was operated using an accelerating voltage of  
206 15 kV with a dwell time of 1500 ms at <200x magnification, yielding an average resolution of <3  $\mu\text{m}$ . Data  
207 correction, deconvolution and element map construction was performed using Oxford Instruments Aztec  
208 software's TruMap function.

### 209 *Mineral chemistry*

210 Laser ablation inductively coupled plasma mass spectrometry (LA-ICP-MS) was carried out on  
211 representative polished mounts ( $n=10$ ) to determine the *in situ* content of trace elements across different  
212 sulfide minerals. In total, 186 spot analyses were carried out across pyrrhotite ( $n=69$ ), pentlandite ( $n=34$ ),  
213 chalcopyrite ( $n=38$ ), and isocubanite ( $n=45$ ; App. Table A1). LA-ICP-MS analysis was performed at  
214 Cardiff University (UK) using a New Wave Research UP213 UV laser coupled to a Thermo iCAP RQ-  
215 ICP-MS. Analysis employed a spot diameter of 55  $\mu\text{m}$  at a frequency of 10 Hz and a gas blank was measured  
216 for 20 s prior to each analysis. Sulfur-33 was used as an internal standard for all analyses and instrument

217 calibration was performed on a series of synthetic Ni-Fe-S standards (see Prichard et al., 2013; Smith et al.,  
218 2016). Data quality was monitored through the repeat analysis of UQAC FeS-1 with calculated relative  
219 standard deviation (RSD) values of <6% for Fe, Ni, Cu, As, Ru, Ag, Te, Re Ir, <10% for Co, Se, Rh, Pt,  
220 Pd, Os, Au and Bi and an RSD of <16% for Zn, Pd, Cd, Sb and Pb (see App. Table A1). Data correction  
221 and the subtraction of gas blanks was performed using Thermo Qtegra software.

### 222 *Sulfur isotope analysis*

223 The sulfur isotope composition of pyrrhotite and chalcopyrite was determined using secondary ion mass  
224 spectrometry (SIMS) microanalysis. Twenty-three analyses were performed across three representative  
225 polished mounts. Epoxy-mounted blocks with aluminum retaining rings were first coated with 300Å of Au  
226 prior to analysis to mitigate charging of the sample during ion bombardment. Samples were analyzed using  
227 a Cameca IMS 4f SIMS instrument at the Microanalysis Facility at Memorial University of Newfoundland  
228 (Canada) following the analytical procedure detailed in Brueckner et al. (2015) and Lode et al. (2017). The  
229 sample was bombarded with a primary ion beam of 350-750 pA of Cs<sup>+</sup>, accelerated through a potential of  
230 10 KeV and focused into a 5-15 µm diameter rastered spot. Negatively charged secondary ions were  
231 accelerated into the mass spectrometer using a potential of +4.5 KeV. To exclude sulfur contamination from  
232 the sample surface, the analytical spot was sputtered for 120 s with a 5-15 µm diameter rastered beam prior  
233 to analysis. All analyses are reported in standard delta notation ( $\delta^{34}\text{S}$ , ‰) relative to Vienna-Canyon Diablo  
234 Troilite (V-CDT). Reproducibility based on the repeat analysis of standard reference material UL9 ( $\delta^{34}\text{S}$ =  
235 16.3‰), KH87 ( $\delta^{34}\text{S}$ = 0.4‰) and PoW1 ( $\delta^{34}\text{S}$ = 3.0‰) is better than 0.4‰ (1 $\sigma$ , see App. Table A2).

### 236 *Sample preparation and analysis of Platinum Group Elements*

237 Samples were prepared for PGE analysis by nickel sulfide fire assay pre-concentration and tellurium co-  
238 precipitation at Cardiff University, as described in Huber et al. (2001), but incorporating the modifications  
239 outlined in McDonald and Viljoen (2006). Solutions were then analyzed for PGE and Au on a Thermo  
240 iCAP RQ-ICP-MS at Cardiff University (UK). Accuracy and precision was assessed by the repeat analysis  
241 of PGE reference material WPR-1 (altered peridotite) (App. Table A3).

242

## Results

### 243 *Mineralogy*

244 Samples from Lakxia tou Mavrou are sub-divided based on texture into veined (Fig. 2 E and F) and massive  
245 samples (Fig. 2G). Veined samples occur surrounding massive sulfide lenses and contain a mesh of sulfide-  
246 rich veins in a serpentinite matrix (Fig. 2E and F). Massive samples contain >95% sulfide minerals, with  
247 minor magnetite, chromite, arsenide minerals and serpentinite (Fig. 2G).

248 *Massive samples.* Massive samples contain pyrrhotite (>95%) with disseminated pentlandite (<5%),  
249 chalcopyrite (<3%) and accessory amounts of chrome spinel, isocubanite, magnetite, and arsenide minerals  
250 (<<1%; see As map in App. 4) (Fig. 3). Pyrrhotite is cross-cut by magnetite-bearing breccia zones (Fig. 3A  
251 and 4) forming along 1-2 mm wide bands of brittle deformation that are surrounded by halos of fingerprint  
252 textured ductilely deformed pyrrhotite (Fig. 3B). Isocubanite occurs as exsolution lamella in chalcopyrite  
253 (Fig. 3C). Chrome spinel occurs as coarse (<0.5 mm) euhedral grains that are disseminated in pyrrhotite  
254 with some grains exhibiting alteration to ferri-chromite at their margins (Fig. 3D). Pentlandite is finely  
255 disseminated throughout the sample and occurs spatially associated with pyrrhotite (Fig. 3E).

256 *Veined samples.* Samples contain isocubanite, chalcopyrite, pentlandite, and pyrrhotite in a matrix of  
257 sheared serpentinite (Fig. 4A and B). Chrome spinel occurs as euhedral grains both surrounded by sulfide  
258 minerals (Fig. 4C) and associated with serpentinite (Fig. 4D). Some chrome spinels are anhedral with a  
259 pitted appearance and have a rim of ferri-chromite alteration (Fig. 4D). Isocubanite is often overgrown by  
260 chalcopyrite at its contact with surrounding serpentinite (Fig. 4E). Chalcopyrite also occurs within massive  
261 isocubanite as orientated exsolution lamella and as later overgrowths forming euhedral grains (Fig. 4F).  
262 Pentlandite occurs in pyrrhotite as discrete micron-scale subhedral grains with a feathery appearance (Fig.  
263 4G and H). Mesh textures of pyrrhotite and chalcopyrite are common (Fig. 4 I, J and K). Some sulfide  
264 grains are fragmented and cross-cut by serpentinite veins. This indicates that brittle deformation of sulfide  
265 minerals took place late in the deposit paragenesis (Fig. 4L).

266 The relationship between sulfide minerals and serpentinite is variable within and between individual  
267 samples (Fig. 5). Clear mineralogical relationships exist between the different minerals in veined samples.  
268 Pentlandite is spatially associated with pyrrhotite, occurring as euhedral grains (Fig. 5A). Isocubanite  
269 occurs in massive zones (Fig. 5A and B) with patchy overgrowths of chalcopyrite (Fig. 5B). The majority  
270 of chalcopyrite occurs localized along shear bands (Fig. 5C). Chrome spinel occurs in all samples as discrete  
271 aggregates associated with serpentinite (Fig. 5). For individual maps of each analyzed element, refer to  
272 Appendix 4.

273 In veined samples, mesh textures are common, and consist of anastomosing networks of mm-scale veins  
274 containing pyrrhotite and chalcopyrite cross-cutting the serpentinite matrix that grade into coherent massive  
275 pyrrhotite and isocubanite (Fig. 5A and B). Evidence of deformation is visible where serpentinite cross-  
276 cuts and offsets pyrrhotite, indicating that displacement has occurred along a shear surface (Fig. 5A). In  
277 other samples, discrete bands of chalcopyrite within serpentinite (+/- chrome spinel) cross-cut isocubanite  
278 and pyrrhotite (Fig. 5C). Clasts of serpentinite within these zones appear to have a crude sigmoidal shape  
279 indicating that localized ductile deformation has occurred post sulfide formation (Fig. 5C), likely during  
280 later NNW-ESE faulting associated with the Pevkos fault.

281 *Dyke-hosted sulfide globules.* Dykes that intrude serpentinite in the vicinity of Lakxia tou Mavrou (Fig. 2A)  
282 contain disseminated poly-sulfide globules. Pyrrhotite, chalcopyrite and pentlandite occur in sub-rounded  
283 globules 2-3 mm in diameter (Fig. 6). One sulfide globule contained predominantly chalcopyrite (Fig. 6A)  
284 whilst all others contain only pyrrhotite with chrome spinel (Fig. 6B). Pentlandite was not visible in any  
285 sample but sub-micron-scale Ni-rich inclusions that are probably pentlandite were visible in some element  
286 maps (Fig. 6C). Euhedral chrome spinel grains occur disseminated within the sulfide globules and in the  
287 zone surrounding the globule (Fig. 6). A halo of Mg-rich alteration of approximately 0.5 to 1 mm wide  
288 mantles all poly-sulfide globules (Fig. 6).

289 *Mineral chemistry*

290 Variations in trace element concentrations are observed between pyrrhotite ( $n=62$ ; spot analyses),  
291 pentlandite ( $n=34$ ), chalcopyrite ( $n=38$ ), isocubanite ( $n=45$ ) and dyke-hosted pyrrhotite ( $n=6$ ). All  
292 analyses returned Ru, Rh, Pd, Os, Ir and Pt concentrations below the detection limit (0.05 to 0.08 ppm).  
293 Metal contents below the detection limit are taken as half the detection limit (see App. Table A1).

294 *Pyrrhotite*. Median contents of Ag, Cd, Sb, As, Pb and Au are below the detection limit in pyrrhotite.  
295 Pyrrhotite contains the lowest median Se and Te content at 111 ppm and 0.41 ppm ( $n=62$ ), respectively  
296 (Fig.7 A and B) and the second highest median Co content and Ni at 349 ppm and 0.17 wt.% ( $n=62$ ; Fig.  
297 7D and F), respectively. A strong positive correlation exists between Co and Ni ( $R^2=0.91$ ; Fig. 7G).

298 *Chalcopyrite*. Chalcopyrite contains the highest median Te, Se, Cd, Sb and Zn contents (Fig. 7). Selenium  
299 is notably enriched with a median content of 213 ppm ( $n=38$ ) and a maximum of 934 ppm (Fig. 7A).  
300 Chalcopyrite has the highest median Te content at 23 ppm ( $n=38$ ; Fig. 7B). A strong positive correlation  
301 exists between Co and Ni ( $R^2 = 0.94$ ; Fig 7G), Zn and Cd ( $R^2=0.95$ ; Fig. 7H) and a weak correlation between  
302 Te and Se ( $R^2=0.58$ ).

303 *Isocubanite*. Isocubanite contains a median Cu content of 25 wt.% ( $n=45$ ; Fig 7E). Isocubanite, with a  
304 median content of 1.3 ppm ( $n=45$ ) is enriched in Ag relative to all other sulfide minerals analyzed.  
305 Isocubanite is depleted in Se relative to chalcopyrite, with a median of 165 ppm ( $n=45$ ; Fig. 7A). A strong  
306 positive correlation exists between Co and Ni ( $R^2=0.85$ ; Fig. 7G) and Cd and Zn ( $R^2=0.84$ ; Fig. 7H).

307 *Pentlandite*. Pentlandite contains the highest median Bi, Sb and As content at 1.0 ppm (Fig. 7C), 0.23 ppm,  
308 and 22 ppm ( $n=34$ ), respectively. The Ni content of pentlandite ranges from 12.7 to 20.7 wt% with a median  
309 of 14.6 wt.% ( $n=34$ ; Fig. 7D). Pentlandite contains an average Co concentration of  $33.0 \pm 5.9$  wt.% ( $1\sigma$ ,  
310  $n=34$ ; 10F). Based on a Co content  $>20$  wt.%, we classify pentlandite as Co-pentlandite (Harris and Nickel,  
311 1972). A strong positive correlation occurs between Ni and Fe ( $R^2 = 0.89$ ) and a moderate negative  
312 correlation between Fe and As ( $R^2=-0.69$ ).

313 *Dyke Pyrrhotite.* Dyke-hosted pyrrhotite has a different trace element signature compared to Lakxia tou  
314 Mavrou pyrrhotite, having a higher Ni, Co, Se, Te and Pb content. Arsenic is enriched in dyke-hosted  
315 pyrrhotite, with a median content of 66 ppm ( $n=6$ ), compared to Lakxia tou Mavrou pyrrhotite, where all  
316 analyses were below the detection limit ( $<1.1$  ppm). Nickel, with a median content of 5641 ppm ( $n=6$ ), is  
317 also enriched relative to Lakxia tou Mavrou pyrrhotite. Concentrations of Cd, Zn, Cu, Ag and Au are below  
318 the detection limit for all analyses. Arsenic exhibits a strong positive correlation with Ni ( $R^2=0.94$ ) and a  
319 moderate positive correlation with Co ( $R^2=0.60$ ).

### 320 *Sulfur isotopes*

321 Sulfur isotope ratios ( $\delta^{34}\text{S}$ ) were measured on pyrrhotite from veined and massive samples ( $n=9$ ) and the  
322 sulfide blebs in the boninite dykes from the serpentinite shear zones ( $n=6$ ) (Fig. 8). Pyrrhotite in massive  
323 samples has an average  $\delta^{34}\text{S}$  value of  $-1.8\pm 1.4\%$  ( $1\sigma$ ,  $n=4$ ; Fig. 8) and pyrrhotite from veined samples -  
324  $2.5\pm 1.5\%$  ( $1\sigma$ ,  $n=5$ ). In contrast, the dyke-hosted pyrrhotite is relatively enriched in  $^{34}\text{S}$ , having an average  
325  $\delta^{34}\text{S}$  value of  $14.7\pm 4.3\%$  ( $1\sigma$ ,  $n=6$ ) and a maximum value of 20.9% (Fig. 8). Chalcopyrite in massive  
326 samples is depleted in  $^{34}\text{S}$  with an average  $\delta^{34}\text{S}$  value of  $-6.1\pm 2.0\%$  ( $1\sigma$ ,  $n=5$ ) relative to veined samples at  
327  $-4.4\pm 2.3\%$  ( $1\sigma$ ,  $n=3$ ) (Fig. 8).

### 328 *Whole rock PGE analysis*

329 Whole rock samples from massive sulfide, veined samples, and from the boninite dykes were analyzed  
330 ( $n=6$ ). All samples have PGE concentrations that are lower than mantle values (mantle values from Palme  
331 and O'Neill, 2003) and only the massive sulfide samples contain Au above mantle values. Massive and  
332 veined samples have similar PGE patterns: flat with a slight positive inflection at Ru, and a strong Au  
333 enrichment. However, the massive samples contain higher concentrations of Ir, Os, Rh, Pt and significantly  
334 higher concentrations of Au than the veined samples (Fig. 9). Massive samples have an average Pt/Pd ratio  
335 of 1.2, Au/Pd ratio of 190.2 and Pd/Ir ratio of 1.7, while veined samples have an average Pt/Pd ratio of 0.8,  
336 Au/Pd ratio of 13.6 and Pd/Ir ratio of 5.5. Boninite dyke samples contain notably less PGE than the  
337 mineralized samples and have a different pattern, with a positive Pt inflection and then a depletion in Au

338 and Pd. Samples from the dykes have an average Pt/Pd ratio of 4.0, Au/Pd ratio of 0.1 and Pd/Ir ratio of  
339 22.1 (Fig. 9; App. Table A3).

## 340 Discussion

### 341 *Magmatic versus hydrothermal origins*

342 Previous studies have suggested either a magmatic (Panayiotou, 1980) or hydrothermal (Foose et al., 1985;  
343 Thalhammer et al., 1986) origin for mineralization at Lakxia tou Mavrou. Mineralization was considered  
344 to have formed through magmatic processes via the segregation of an immiscible sulfide liquid during the  
345 ascent of basaltic melts through the lower crust (Panayiotou, 1980). This genetic model was based primarily  
346 on the absence of a hydrothermal alteration halo surrounding the sulfide mineralization and the enrichment  
347 of Cu with Cu/Cu+Ni of between 0.16 and 0.47 (Panayiotou, 1980).

348 Later studies have suggested a hydrothermal origin for the mineralization, where metals are sourced from  
349 the serpentinization of mantle peridotites (Foose et al., 1985; Thalhammer et al., 1986). If mineralization  
350 were formed via purely magmatic processes, as suggested by Panayiotou (1980), it would be expected to  
351 have a Pt/(Pt+Pd) ratio of between 0.2 and 0.4; however Pt/(Pt+Pd) ratios are elevated at Lakxia tou  
352 Mavrou, ranging between 0.51-0.66 (Foose et al., 1985). Sulfide mineralization is also depleted in PGEs  
353 relative to Troodos gabbros and peridotites, with a flat PGE profile and a sharp increase in Au, again  
354 suggesting a hydrothermal origin (Foose et al., 1985). Thus, a two-step hydrothermal model explaining the  
355 formation of Lakxia tou Mavrou sulfide mineralization was instead proposed: (i) high-temperature fluids  
356 (400-500°C) formed pyrrhotite-rich mineralization with co-precipitated arsenide minerals followed by, (ii)  
357 a lower temperature (200-300°C) fluid that precipitated Cu-rich sulfide minerals (Thalhammer et al., 1986).

358 All of these models were proposed before detailed mapping and geological investigation of the Limassol  
359 Forest Complex (Murton, 1986a, b; MacLeod, 1988, 1990; MacLeod and Murton 1993, 1995; Gass et al.,  
360 1994), and without the benefits these studies brought in deciphering the detailed geological context of the

361 Lakxia tou Mavrou area. The origin and paragenesis of the mineralization is re-evaluated in this study by  
362 applying a combined mineralogical, geochemical and isotopic approach.

### 363 *Evidence of a hydrothermal origin for Lakxia tou Mavrou*

364 Firstly, S/Se ratios are commonly used to constrain the source of sulfur in magmatic and hydrothermal ore  
365 deposits (Yamamoto, 1976; Queffurus and Barnes, 2015; Smith et al., 2016). The S/Se ratio of the mantle  
366 is between 2850 to 4350 (Eckstrand and Hulbert, 1987). At Lakxia tou Mavrou the median S/Se for all  
367 sulfide minerals are 2293 ( $n=180$ ) with a range of 304 to 108,571, which is comparable to hydrothermal  
368 mineral deposits where the S/Se ratios range from 3500 to 100,000 (Yamamoto, 1976; Huston et al., 1995;  
369 Hannington et al., 1999; Layton-Matthews et al., 2013). Therefore, S/Se ratios that are highly variable and  
370 plot both above and below mantle values support a hydrothermal origin for mineralization at Lakxia tou  
371 Mavrou.

372 The sulfur isotope composition of Troodos mantle rocks is between 0-1‰ (Alt 1994). Therefore, if  
373 mineralization at Lakxia tou Mavrou did form through magmatic processes, then the sulfur isotope  
374 composition of sulfide minerals should also be similar (e.g., Smith et al., 2016). Instead, the average  $\delta^{34}\text{S}$   
375 values for all sulfide minerals analyzed in this study is  $-3.7\pm 2.4\text{‰}$  ( $1\sigma$ ,  $n=17$ ) ranging from  $-7.9\text{‰}$  to -  
376  $0.1\text{‰}$ , values that are largely not compatible with a magmatic origin (Smith et al., 2016).

377 Additional whole-rock PGE concentration data for veined, massive, and dyke-hosted sulfide globules also  
378 support a hydrothermal origin for Lakxia tou Mavrou (Fig. 9). Massive and veined samples have a similar  
379 chondrite-normalized PGE profile with a positive Ru inflection and slight negative inflection at Pt and both  
380 massive and veined samples are enriched in Au relative to primary Troodos host rocks. Platinum/(Pt+Pd)  
381 values for Lakxia tou Mavrou sulfides from this study range from 0.39 to 0.55 (average = 0.50,  $n=4$ ) and  
382 are in good agreement with two previously published values of 0.51 and 0.66 (Naldrett et al., 1979; Foose  
383 et al., 1985). Platinum group element data (Table 2) indicate that the sulfide minerals are depleted in PGE



384 when compared to mantle concentrations, further supporting the premise that the sulfide minerals are either  
385 of hydrothermal origin or have been leached during later hydrothermal processes (Naldrett et al., 1979).  
386 These data indicate that mineralization at Lakxia tou Mavrou does not have a simple magmatic origin  
387 through the segregation of an immiscible sulfide liquid. However, the relationship between serpentinization,  
388 faulting, fluid flow, the formation of sulfide mineralization and source of metals remain poorly constrained.  
389 To investigate this further we conducted *in situ* geochemical and sulfur isotope analysis, and draw  
390 comparisons between SMS deposits hosted in ultramafic rocks, Outokumpu-type VMS deposits and Lakxia  
391 tou Mavrou to examine if mineralizing processes are comparable.

### 392 *Metal and sulfur sources at Lakxia tou Mavrou*

393 *Serpentinization.* Serpentinization, which occurs when primary olivine and pyroxene are hydrated to form  
394 secondary minerals such as lizardite, chrysotile and magnetite, produces geochemically distinct fluids  
395 (Klein and Bach, 2009). Fluids produced during serpentinization are highly reduced, alkaline and have a  
396 low  $fS_2$  (e.g., Allen and Seyfried, 2003). Serpentinization reactions are exothermic (MacDonald and Fyfe,  
397 1985) and may drive hydrothermal fluid circulation (Rona et al., 1987). Modeling indicates that  
398 serpentinization can produce temperatures of up to ~260 °C, however, low fluid flow rates ( $\leq 10$  kg/s) or  
399 high rates of serpentinization ( $\geq 100$  kg/s) are required to reach these temperatures (Lowell and Rona,  
400 2002). To achieve temperatures of  $>300^\circ\text{C}$ , similar to temperatures recorded in basalt-hosted SMS systems  
401 (Hannington et al., 2005) an additional heat source (i.e., magmatic intrusions) is needed (Lowell and Rona,  
402 2002). For example, even at the Lost City hydrothermal field (MAR: Denny et al., 2016; Kelley et al., 2001;  
403 Früh-Green et al., 2003) low-temperature (~40-91 °C), high-pH (9-9.8) and metal-poor fluids are thought to  
404 be influenced by the presence of mafic intrusions (Allen and Seyfried, 2004). In ultramafic-hosted vent  
405 sites where fluid temperatures are higher due to the presence of mafic intrusions below the seafloor (e.g.,  
406 Rainbow; 364 °C), high  $H_2$  contents (16 mmol/kg) have been measured in vent fluid, that are produced  
407 during serpentinization (Charlou et al., 2002). In these higher temperature systems, accumulations of sulfide  
408 minerals occur at the seafloor (e.g., Rainbow, Logatchev, Semenov). Sulfide accumulation reflects the

409 increased solubility of many metals (e.g., Cu) in high-temperature and low-pH hydrothermal fluid  
410 (Rainbow; 365°C, pH 2.8; Charlou et al., 2002) (Palandri and Reed, 2004). Consequently, low-S, high-Fe  
411 mineral assemblages containing isocubanite and pyrrhotite form due to the occurrence of reduced, sulfur  
412 poor fluids, and have been reported in some ultramafic-hosted SMS deposits (Firstova et al., 2016).  
413 Serpentinization in the STTFZ occurred on/below the ocean-floor and has been discussed in detail by  
414 Murton (1986a,b), MacLeod & Murton, (1993, 1995) and Gass et al. (1994). Hence, in the context of  
415 mineralization at Lakxia tou Mavrou, serpentinization could provide a source of metals.

416 The mineral assemblage, consisting of pyrrhotite and isocubanite (+/- chalcopyrite) at Lakxia tou Mavrou  
417 indicates that fluids had a low  $fS_2$  and were highly-reduced, favoring the formation of pyrrhotite over pyrite,  
418 and isocubanite over chalcopyrite (Klein and Bach, 2009; Firstova et al., 2016). The highly reducing fluid  
419 conditions are a consequence of serpentinization and redox reactions related to olivine and orthopyroxene  
420 dissolution (Moody, 1976). At Lakxia tou Mavrou the pyrrhotite-rich sulfide mineral assemblage indicates  
421 the involvement of high-temperature (200-500°C) highly-reduced fluids (Thalhammer et al., 1986), and  
422 consequently, an additional source of heat at Lakxia tou Mavrou, in the form of gabbroic intrusions and  
423 cross-cutting dykes is needed to produce sufficient amounts of heat to form sulfide mineralization.

424 Geochemical proxies such as the ratio of Co/Ni in Lakxia tou Mavrou sulfide minerals support the  
425 contribution of metals from an ultramafic source (e.g., Marques et al., 2006). The median Ni and Co content  
426 of pyrrhotite at Lakxia tou Mavrou is 68 and 178 times higher (Table 1), respectively for Ni and Co  
427 compared to the median content in pyrite from all Troodos VMS deposits ( $n=1376$ ; Keith et al., 2016;  
428 Martin et al., 2019, 2020). This reflects the higher primary content of Ni and Co in peridotites, globally,  
429 with mean concentrations of 2,344 ppm and 109 ppm, respectively (Gülaçar and Delaloye, 1976) compared  
430 to mid-ocean ridge basalts that contain 92 ppm and 43 ppm Ni and Co, respectively (Gale et al., 2013). The  
431 enrichment of Ni and Co at Lakxia tou Mavrou relative to basaltic-hosted VMS deposits provides evidence  
432 for hydrothermal fluids at high-temperatures (>300°C) interacting with ultramafic lithologies.

433 At Lakxia tou Mavrou the average Co/Ni ratio for pyrrhotite is 3.4 ( $n=62$ ), whilst the Co/Ni ratio from  
434 pyrite at Skouriotissa, a basalt-hosted VMS deposit in Troodos is 6.9 ( $n=43$ ; Martin et al., 2019) (Fig. 10).  
435 Thus, the low Co/Ni ratio of pyrrhotite at Lakxia tou Mavrou combined with their elevated concentration,  
436 relative to the Skouriotissa VMS deposit, supports the contribution of metals from an ultramafic source  
437 rock. The average Co/Ni ratio of 3.4 ( $n=62$ ) that lies between peridotite and mafic lithologies indicates a  
438 mixed mafic and ultramafic source of metals at Lakxia tou Mavrou (Fig. 10).

439 *The role of mafic intrusions.* In the western Limassol Forest, in the broader vicinity of Lakxia tou Mavrou,  
440 Transform Sequence wehrlite and gabbro plutons, plus associated (locally sheeted) swarms of boninitic  
441 dykes intrude into the serpentized mantle, in places accommodating up to 22% of extension (Fig. 1B;  
442 Murton, 1986a; Gass et al., 1994). Transform Sequence dykes and gabbroic intrusions are clearly significant  
443 locally as a source of heat and metals (Murton 1986a, b; MacLeod and Murton, 1993, 1995; Gass et al.,  
444 1994). Early Transform Sequence dyke generations provide evidence of interaction with high-temperature  
445 ( $\sim 350^\circ\text{C}$ ) hydrothermal fluids and are altered to greenschist to lower amphibolite facies (Murton et al.,  
446 1986a). Mass balance calculations in the main Troodos Massif show that at greenschist temperatures, metals  
447 are effectively leached from dyke material (Jowitt et al., 2012), hence, we suggest similar such processes  
448 occurred in the vicinity of Lakxia tou Mavrou with mafic intrusions providing an additional source of some  
449 metals.

450 Mafic lithologies may have also played an important role in lowering fluid pH and thus enhancing metal  
451 solubility (Palandri and Reed, 2004). This relates to the formation of chlorite, drawing Al from mafic  
452 lithologies and  $\text{Mg}^{2+}$  from seawater, producing  $\text{H}^+$  ions, lowering the pH of the hydrothermal fluid (Seyfried  
453 and Mottl, 1982). This reaction can overwhelm the brucite buffer that occurs during serpentization, and in  
454 addition to heat generated from the intrusion itself, will enhance the solubility of metals in the hydrothermal  
455 fluid (Palandri and Reed, 2004). Chloritization is prominent in gabbro intrusions, wehrlite bodies and  
456 cross-cutting Transform Sequence dykes in the Limassol Forest Complex indicating that the formation of  
457 chlorite was an important mechanism in producing low-pH hydrothermal fluids.

458 Data from this study provides further evidence of hydrothermal alteration in the syn-tectonic boninitic  
459 Transform Sequence dykes. The sulfur isotopic signature of disseminated pyrrhotite hosted within  
460 Transform Sequence dykes ( $14.7 \pm 4.3\text{‰}$   $1\sigma$ ,  $\text{max} = 20.9\text{‰}$ ;  $n=6$ ) are distinctly different from both Troodos  
461 VMS deposits, sulfide minerals at Lakxia tou Mavrou and the magmatic mean for Troodos igneous rocks  
462 ( $0\text{--}1\text{‰}$ ; Alt 1994) (Fig. 8). If these sulfide globules formed through primary magmatic processes then the  
463  $\delta^{34}\text{S}$  values should plot around the Troodos magmatic mean of  $0\text{--}1\text{‰}$  (Alt 1994). Instead the average  $\delta^{34}\text{S}$   
464 value in pyrrhotite is significantly higher, indicating that the sulfide globules cannot be of a simple  
465 magmatic origin. Furthermore, the dykes have a positive chondrite normalized PGE slope but are depleted  
466 in Pd and Au relative to Lakxia tou Mavrou bulk-rock massive and veined samples (Fig. 9). These PGE +  
467 Au signatures are different to those analyzed in sulfide-bearing gabbros from the main Troodos Massif,  
468 which exhibit a positive slope with a trough in Ru and a peak in Pd relative to the dykes in this study  
469 (Prichard and Lord, 1990; Fig. 9). Therefore we deduce that the geochemical signature of the sulfide  
470 globules in the dykes must have been modified during the leaching of metals during hydrothermal alteration  
471 and rodingitization, leaving globules depleted in PGE relative to primary magmatic sulfide minerals.  
472 Alteration halos surrounding the sulfide globules (Fig. 6) further support that leaching and replacement has  
473 occurred. Thus, we suggest that hydrothermal alteration of mafic intrusions provided an additional source  
474 of metals, heat and probably played an important role in lowering fluid pH during the formation of sulfide  
475 mineralization at Lakxia tou Mavrou.

476 *Sulfur sources.* The sulfur isotopic composition of sulfide minerals at Lakxia tou Mavrou is below the  
477 Troodos magmatic mean of  $0\text{--}1\text{‰}$  (Alt 1994). An average  $\delta^{34}\text{S}$  value of  $-3.7 \pm 2.4\text{‰}$  ( $1\sigma$ ,  $n=17$ ) is not  
478 compatible with sulfur sourced from a mixture of thermochemical sulfate reduction (TSR) of seawater and  
479 the leaching of sulfur from igneous lithologies without any additional fractionation processes, as this would  
480 produce sulfide minerals with  $\delta^{34}\text{S}$  values  $>0\text{‰}$ , such as those measured in ultramafic-hosted SMS deposits  
481 (Fig. 11).

482 Measured  $\delta^{34}\text{S}$  values in pyrite that are lower than the Troodos magmatic mean have previously been  
483 documented at the basalt-hosted Mala VMS deposit (Troodos), where the median  $\delta^{34}\text{S}$  value of pyrite is -  
484 4.6‰ ( $n=28$ , Martin et al., 2021) (Fig. 11). At Mala, that is interpreted to represent an immature VMS  
485 deposit,  $\text{SO}_2$  from degassing shallow magma chambers undergoes disproportionation, producing low  $\delta^{34}\text{S}$   
486 values in pyrite that are  $<0\text{‰}$  (Martin et al., 2021). The addition of a magmatic volatile phase to the  
487 hydrothermal system at Lakxia tou Mavrou is unlikely as mineralization is associated with ultramafic  
488 lithologies that are volatile poor (especially with respect to  $\text{SO}_2$ ) relative to felsic lithologies. However, the  
489 addition of magmatic volatiles cannot be excluded as boninitic dykes that occur surrounding Lakxia tou  
490 Mavrou could potentially contribute magmatic volatiles. We do not consider microbial sulfate reduction  
491 (MSR) of seawater or sulfur leached from igneous host rocks at Lakxia tou Mavrou as a plausible source  
492 of isotopically light sulfur, as MSR occurs at low-temperatures ( $\ll -122^\circ\text{C}$ ; Takai et al., 2008) that are not  
493 consistent with the high-temperature ( $>200^\circ\text{C}$ ) sulfide mineral assemblage at Lakxia tou Mavrou.

494 At Lakxia tou Mavrou sulfur isotope ratios of sulfide minerals increase from  $-7.9\text{‰}$  in massive sulfide  
495 mineralization to  $20.9\text{‰}$  in dyke-hosted sulfide globules and are evidence of increasing amounts of TSR at  
496 different stages along a fluid pathway through the crust. As seawater penetrates down the shear zone it  
497 becomes heated by underlying magmatic intrusions and, at temperatures  $>150^\circ\text{C}$ , anhydrite precipitation  
498 occurs (Fig. 12; Blounot and Dickson, 1969). Any remaining sulfate in the hydrothermal fluid is transported  
499 to deeper crust levels and, at temperatures  $>250^\circ\text{C}$  and in the presence of iron-bearing minerals, is  
500 thermochemically reduced to  $\text{H}_2\text{S}$  (Machel et al., 1995). The equilibrium isotopic fractionation between  
501  $\text{SO}_4^{2-}$  and  $\text{H}_2\text{S}$  is temperature dependent, with a greater degree of fractionation occurring at lower  
502 temperatures (Ohmoto and Rye, 1979). The amount of fractionation between  $\text{H}_2\text{S}$ , pyrrhotite and  
503 chalcopyrite is typically  $<0.8\text{‰}$  at temperatures  $>300^\circ\text{C}$  and is therefore minor (Li and Liu, 2006). During  
504 the TSR process, degree of progress of the sulfate reduction can be expressed in terms of  $f$  values, where  $f$   
505 =  $[\text{H}_2\text{S}]_{\text{SR}}/[\text{SO}_4]^0$ , and  $[\text{H}_2\text{S}]_{\text{SR}}$  denotes  $\text{H}_2\text{S}$  generated during TSR and  $[\text{SO}_4]^0$  is the initial sulfate  
506 concentration of the fluid (Dubinina et al., 2020; Ono et al., 2012).

507 Low sulfur isotope values ( $<0\%$ ) at Lakxia tou Mavrou are produced during the initial stage of TSR at low  
508  $f$  values ( $\sim 0.1$ ) where only a small proportion of the sulfate entering the hydrothermal system undergoes  
509 TSR (Fig. 12). Equilibrium fractionation factors between  $\text{SO}_4^{2-}$  and  $\text{H}_2\text{S}$  are  $22.2\%$  at a temperature of  
510  $300^\circ\text{C}$  (Sakai, 1968), forming sulfide minerals with negative  $\delta^{34}\text{S}$  values down to  $-7.9\%$  at Lakxia tou  
511 Mavrou (Fig. 12). Continued TSR (i.e., increasing  $f$  values) of the same fluid enrich the remaining sulfate  
512 in  $^{34}\text{S}$  relative to the initial composition of seawater sulfate ( $\sim 18\text{-}19\%$ ; Kampschulte and Strauss, 2004).  
513 Continued TSR in a semi-closed system (with respect to seawater recharge) forms sulfide minerals with  
514 increasingly higher  $\delta^{34}\text{S}$  values as sulfate that undergoes TSR is progressively enriched in  $^{34}\text{S}$  but the  
515 equilibrium fraction factor remains constant at a given temperature (i.e.,  $\sim 22.2\%$  at  $300^\circ\text{C}$ ). High  $\delta^{34}\text{S}$   
516 values such as those reported in dyke-hosted pyrrhotite globules that average  $14.7 \pm 4.3\%$  ( $1\sigma$ ,  $n=6$ ) are  
517 produced by near complete TSR at high  $f$  values ( $f = \sim 0.9$ ). Therefore, variation in  $\delta^{34}\text{S}$  values between  
518 sulfide minerals at Lakxia tou Mavrou and dyke-hosted pyrrhotite indicate progressively greater degrees of  
519 TSR in a semi-closed system that occurred along a fluid flow pathway (Fig. 12). At Lakxia tou Mavrou  
520 only the initial and end stage of TSR, representing low ( $\sim 0.1$ ) and high ( $\sim 0.9$ )  $f$  values, respectively are  
521 preserved. Intermediate  $f$  values that will form sulfide minerals with  $\delta^{34}\text{S}$  values of between  $\sim 0\text{-}10\%$  are  
522 absent in the samples analyzed. We propose that the absence of these values is due to a sampling bias and  
523 suggest that values between  $0\text{-}10\%$  would be preserved in more distal parts of the mineralization, possibly  
524 toward Pevkos. Thus, the sulfur isotope composition of sulfide minerals at Lakxia tou Mavrou remains  
525 somewhat enigmatic, nevertheless we show that sulfur isotope systematics are distinctly different to those  
526 typical of actively-forming ultramafic SMS deposits and other basalt-hosted Troodos VMS deposits.

### 527 *Sulfide mineralization in an ancient transform fault zone*

528 Initially metals at Lakxia tou Mavrou were sourced from the serpentinization of peridotites in the vicinity  
529 of E-W trending vertical strike-slip shear zones, where seawater preferentially exploited the increased  
530 permeability related with deep-seated fault structures during fault movement from a very early stage (Fig.  
531 13 - T1; MacLeod and Murton, 1993; Fagereng and MacLeod, 2019; Cox et al., 2021). The heat generated

532 during exothermic serpentinization reactions was insufficient to form significant accumulations of massive  
533 sulfide mineralization. Despite the relatively low-temperatures (<100°C), Ni and Co would have been  
534 leached during serpentinization (Fig. 13; T1).

535 Transform Sequence wehrlitic and gabbroic plutons and associated dyke swarms were intruded into already  
536 pervasively serpentinized peridotites in the vicinity of E-W trending transform shear zones in the  
537 lithospheric mantle. Decompressive partial melting was generated during trans-tension within/across the  
538 active transform portion of the STTFZ and intrusions provided an additional source of heat that drove  
539 convection of seawater-derived hydrothermal fluids. This produced an initial high-temperature (400-500°C;  
540 Thalhammer et al., 1986) stage of pyrrhotite-rich mineralization at Lakxia tou Mavrou (Fig. 13; T2). The  
541 solubility of Ni and Co, which had been liberated to form sulfide mineralization as a result of earlier and  
542 ongoing serpentinization increases at high-temperatures and low fluid pH as both Ni and Co possess an  
543 increased affinity for fluids >350°C (Liu et al., 2011, 2012). In addition to the mobilization of metals  
544 released during serpentinization, the addition of some metals from Transform Sequence intrusions (gabbros,  
545 wehrlites and dykes) also occurred (Fig. 13; T2). Within the roof zone of gabbroic stocks, aplite apophyses  
546 exhibit evidence of pervasive hydrothermal alteration with primary minerals being replaced by epidote,  
547 chlorite and actinolite (Murton 1986b), thus providing evidence that gabbroic plutons in the vicinity of  
548 Lakxia tou Mavrou (Fig. 1B and C) could have provided a source of metals.

549 Precipitation of sulfide minerals occurred in areas of increased permeability where seawater-derived  
550 hydrothermal fluids mixed with a down welling lower temperature seawater-derived fluid in the vicinity of  
551 E-W trending shear zones (Fig. 13; T2 inset image). This led to a decrease in fluid temperature and an  
552 increase in pH and  $fO_2$  precipitating sulfide minerals. The continued intrusion of Transform Sequence  
553 dykes, that are variably altered from early amphibolite-greenschist dykes to brownstone facies dykes  
554 (Murton et al., 1986a) indicate prolonged hydrothermal and magmatic activity (Fig. 13; T3). As the initial  
555 gabbro and wehrlite intrusions cooled, ongoing dyke intrusions provided both a source of heat that drove  
556 prolonged high-temperature (>250°C) fluid circulation as well as providing an additional source of metals

557 (e.g., Cu) and buffering fluid pH to low values (~2) due to Mg sequestration from seawater derived  
558 hydrothermal fluids . Early Ni and Co-rich mineral assemblages are overprinted by isocubanite and later  
559 by chalcopyrite (Fig. 13; T3). The transition towards more Cu-rich mineral assemblages indicates a  
560 decrease in the temperature of hydrothermal circulation from ~400°C to ~250°C and the introduction of a  
561 higher proportion of metals sourced from Transform Sequence dykes that were intruded contemporaneously  
562 with the formation of Cu-rich sulfide mineralization (Fig. 13; T3; Thalhammer et al., 1986). A decrease in  
563 fluid temperature is also evident in the decreasing alteration intensity and rodingitization of Transform  
564 Sequence dykes, with the youngest “brownstone” dykes appearing less-altered relative to earlier  
565 amphibolite facies dykes (Murton 1986b). The proposed three-stage interpretation presented in this study  
566 for Lakxia tou Mavrou effectively links mineralogical, geochemical and isotopic observations to the  
567 tectonic and magmatic evolution of the Limassol Forest Complex and the accumulation of sulfide minerals  
568 below the seafloor.

569 The entire mineralized package at Lakxia tou Mavrou has later been affected by deformation events related  
570 to the younger the Pevkos fault leading to the localization of sulfide mineralization along WNW-trending  
571 structures, and hence to post-ocean-floor dismemberment of sulfide mineralization during faulting (Fig.  
572 1A and B). This interpretation is implicit in previous work (Panayiotou, 1980; Foose et al., 1985;  
573 Thalhammer et al., 1986). However, given the extreme weakness of both the host serpentinite and sulfide  
574 minerals, and considering the combination of magmatism and high-temperature hydrothermal fluid  
575 conditions required to generate the mineral concentrations of this type, we propose that the apparent  
576 association of sulfide mineralization with WNW faulting is a secondary effect, and is not related to  
577 transform related E-W deformation and serpentinite shear zone formation.

### 578 *An analogue for ultramafic-hosted SMS or Outokumpu-type VMS deposits?*

579 Sulfide mineralization at Lakxia tou Mavrou provides insights into sub-seafloor processes in ultramafic-  
580 hosted SMS deposits. The area surrounding Lakxia tou Mavrou, specifically the hydrothermal alteration of



581 dykes and gabbroic plutons, the depletion of dykes in PGE's relative to mantle values and the high  $\delta^{34}\text{S}$   
582 values in sulfide blebs provides evidence that gabbroic intrusions and cross-cutting dykes are a source of  
583 metals and heat, a relationship that is only inferred in ultramafic-hosted SMS deposits (e.g., Petersen et al.,  
584 2009). The occurrence of Co-Pentlandite and chrome spinel at Lakxia tou Mavrou is comparable to  
585 ultramafic SMS deposits, with chrome spinel forming through the replacement of peridotite host rocks  
586 (Marques et al., 2006, Borodaev et al., 2007; Fouquet et al., 2010), supported at Lakxia tou Mavrou by the  
587 abundance of mesh textured sulfides. However, the occurrence of pyrrhotite and isocubanite at Lakxia tou  
588 Mavrou, that are comparatively rare in SMS deposits indicate that fluids had a lower  $f\text{S}_2$  at Lakxia tou  
589 Mavrou relative to those typical in ultramafic-hosted SMS deposits (Firstova et al., 2016). Sulfur isotope  
590 ratios of sulfide minerals at Lakxia tou Mavrou show that limited mixing between seawater and  
591 hydrothermal fluids occurred, indicating the system was semi-closed with respect to seawater influx. This  
592 is distinctly different to SMS deposits, which are located at or near the seafloor where seawater mixing with  
593 hydrothermal fluid readily occurs producing largely positive  $\delta^{34}\text{S}$  values in SMS deposits (Fig. 11). Largely  
594 the variation in sulfur isotope composition is a consequence of the formation of Lakxia tou Mavrou at  
595 deeper crustal depths (~3 km) where seawater mixing was more restricted. Given the amount of erosion  
596 (~3-4 km) that occurred in the Limassol Forest Complex, it remains unclear if Lakxia tou Mavrou sulfide  
597 mineralization once outcropped on the seafloor.

598 When comparing between Lakxia tou Mavrou and Outokumpu-type VMS deposits, clear differences and  
599 similarities exist. Firstly, sulfide mineralogy is comparable between deposit types, with isocubanite,  
600 pyrrhotite and arsenide minerals forming common mineral phases (Thalhammer et al., 1986; Peltonen et  
601 al., 2008). In Outokumpu-type deposits, solid-state remobilization of metals during metamorphism is  
602 inferred to be an important process in concentrating Ni, whereby Ni is remobilized from surrounding  
603 disseminated mineralization into massive ore zones (Peltonen et al., 2008). This remobilization leads to the  
604 formation of "proto" Cu-rich ore that is overprinted by later Ni-rich mineral assemblages (e.g., at  
605 Outokumpu). At Lakxia tou Mavrou, metamorphic overprinting, besides deformation that occurred within

606 the seafloor transform zone is minor or absent. Nickel, which is concentrated in Co-pentlandite and  
607 associated with pyrrhotite at Lakxia tou Mavrou occurred early in the deposit paragenesis and is associated  
608 with an initial high-temperature phase of fluid flow, and is not related to later metamorphic remobilization  
609 (Thalhammer et al., 1986). Trace metal signatures at Lakxia tou Mavrou are broadly comparable to those  
610 reported in Outokumpu-type VMS deposits that are depleted in Sb, Bi and Pb, reflecting the lower content  
611 of these elements in ultramafic compared to mafic and felsic lithologies (Peltonen et al., 2008).

612 Mineralizing processes at Lakxia tou Mavrou appear to be a hybrid between ultramafic-hosted SMS  
613 deposits and Outokumpu-type VMS deposits. The well-constrained tectonic environment in which Lakxia  
614 tou Mavrou formed suggests that seafloor transform fault zones are a plausible environment for the  
615 formation of Outokumpu-type deposits, however subsequent metamorphism is required to upgrade metal  
616 tenors and form a “typical” Outokumpu-type deposit. Furthermore, our data indicates that whilst similarities  
617 do exist between ultramafic-hosted SMS deposits and Lakxia tou Mavrou, the environment of formation  
618 was different. Lakxia tou Mavrou formed at much deeper crustal depths in the region of ~3 km. Lakxia tou  
619 Mavrou does however provide a useful and readily accessible analogue to understand the role of mafic  
620 intrusions as a source of heat and metals in ultramafic-hosted SMS deposits.

## 621 **Summary and conclusions**

622 At Lakxia tou Mavrou sulfide minerals have an average sulfur isotope ( $\delta^{34}\text{S}$ ) composition of  $<0\%$ , S/Se  
623 ratios that are highly variable and a depletion in PGE's with an enrichment in Au indicating that  
624 mineralization formed through hydrothermal processes. When compared with traditional VMS/SMS  
625 deposits that form at or near the seafloor, mineralization at Lakxia tou Mavrou formed at deeper crustal  
626 levels, ~3-4 km below the seafloor, highlighting the potential for replacement-style mineralization deep  
627 below the seafloor in transform fault zones. The occurrence of Co-pentlandite, pyrrhotite and isocubanite  
628 and enrichment of all sulfide minerals in Ni and Co relative to basalt-hosted VMS deposits in Troodos  
629 indicate a Co and Ni enriched source such as the serpentinization of mantle peridotites. Transform Sequence

630 dyke and gabbro intrusions played an important role in generating heat and acidity to drive prolonged high-  
631 temperature low-pH hydrothermal circulation at Lakxia tou Mavrou. Sulfide blebs within these dykes  
632 contain very high  $\delta^{34}\text{S}$  values, are depleted in PGE's relative to Troodos magmatic rocks and contain  
633 alteration rims, indicating the leaching of sulfide minerals in dykes provided and additional source of metals  
634 at Lakxia tou Mavrou.

635 Whilst some aspects of the sulfide mineralization at Lakxia tou Mavrou are comparable to SMS deposits  
636 hosted in ultramafic rocks, such as mineralogy and sulfide geochemistry, the mineralizing processes are not  
637 analogous between the two environments. This is especially true when considering sulfur isotope  
638 systematics where the  $\delta^{34}\text{S}$  composition of Lakxia tou Mavrou sulfide minerals indicate that progressive  
639 TSR of seawater took place in a semi-closed system compared to open system conditions at the seafloor  
640 during SMS deposit formation. Our study confirms the importance of mafic intrusions as a source of heat  
641 and metals in sub-seafloor replacement-style sulfide mineralization in ultramafic rocks on the seafloor.  
642 Furthermore, we highlight the potential to form Outokumpu-type sulfide deposits below the seafloor in  
643 transform fault zones that are affected by late magmatic intrusions. A hybrid model between ultramafic-  
644 hosted SMS deposits and Outokumpu-type VMS deposits best explains the style of mineralization at Lakxia  
645 tou Mavrou and bridges the gap between these two deposit types.

## 646 Acknowledgments

647 This work was funded by the Natural Environment Research Council (NERC) grant  
648 NE/M010848/1 "TeaSe: Tellurium and Selenium Cycling and Supply" awarded to Cardiff University. JWW  
649 acknowledges the support of the Canadian Research Chair program. The authors acknowledge the support  
650 of Andreas Zissimos from the Geological Survey Department of Cyprus. We thank Michael Green for his  
651 assistance in the field. Duncan Muir is thanked for his assistance on the SEM. Graham Layne and Glenn  
652 Piercey of the Micro Analysis Facility at Memorial University of Newfoundland are thanked for their  
653 assistance during SIMS analysis. We thank Mark Hannington and Hannah Grant for their constructive

654 reviews. We thank associate editor Jonathan Cloutier and editor-in-chief Larry Meinert for the editorial  
655 handling of this manuscript.

## 656 **References**

657 Allen, D.E., Seyfried, W.E., 2003, Compositional controls on vent fluids from ultramafic-hosted  
658 hydrothermal systems at mid-ocean ridges: An experimental study at 400°C, 500 bars:  
659 *Geochimica et Cosmochimica Acta*, v. 67, p. 1531–1542.

660 Allen, D.E., Seyfried, W.E., 2004, Serpentinization and heat generation: constraints from Lost City and  
661 Rainbow hydrothermal systems: *Geochimica et Cosmochimica Acta*, v. 68, p. 1347–1354.

662 Alt, J.C., 1994, A sulfur isotopic profile through the Troodos ophiolite, Cyprus: Primary composition and  
663 the effects of seawater hydrothermal alteration: *Geochimica et Cosmochimica Acta*, v. 58, p.  
664 1825–1840.

665 Alt, J.C., Shanks, W.C., 2003, Serpentinization of abyssal peridotites from the MARK area, Mid-Atlantic  
666 Ridge: sulfur geochemistry and reaction modeling: *Geochimica et Cosmochimica Acta*, v. 67, p.  
667 641–653.

668 Blounot, C.W., Dickson, F.W., 1969, The solubility of anhydrite (CaSO<sub>4</sub>) in NaCl-H<sub>2</sub>O from 100 to  
669 450°C and 1 to 1000 bars: *Geochimica et Cosmochimica Acta*, v. 33, p. 227–245.

670 Bogdanov Y.A., Bortnikov N.S., Vikentev I.V., Gurvich E.G., Sagalevich A.M., 1997, A new type of  
671 modern mineral-forming system: Black smokers of the hydrothermal field at 14°45'N latitude,  
672 mid-atlantic ridge: *Geology of Ore Deposits*, v. 39, p. 57-87.

673 Bogdanov Y.A., Bortnikov N.S., Vikentev I.V., Lein Y.A., Gurvich E.G., Sagalevich A.M., Simonov  
674 V.A., Ikoskii S.V., Stavrova O.O., Apollonov V.N., 2002 Mineralogical-Geochemical  
675 Peculiarities of Hydrothermal Sulfide Ores and Fluids in the Rainbow Field Associated with  
676 Serpentinites, Mid-Atlantic Ridge (36°14' N): *Geology of Ore Deposits*, v. 44, p. 444-473.

677 Borodaev, Yu.S., Bryzgalov, I.A., Mozgova, N.N., Uspenskaya, T.Yu., 2007, Pentlandite and Co-  
678 enriched pentlandite as characteristic minerals of modern hydrothermal sulfide mounds hosted by  
679 serpentinized ultramafic rocks (Mid-Atlantic Ridge): Moscow University Geological Bulletin, v.  
680 62, p. 85–97.

681 Brazilian Metals Group 2015, Annual Report 2015, ([www.bmgl.com.au/investors/annual-reports](http://www.bmgl.com.au/investors/annual-reports)).

682 Brueckner, S.M., Piercey, S.J., Layne, G.D., Piercey, G., Sylvester, P.J., 2015, Variations of sulphur  
683 isotope signatures in sulphides from the metamorphosed Ming Cu(–Au) volcanogenic massive  
684 sulphide deposit, Newfoundland Appalachians, Canada: Mineralium Deposita, v. 50, p. 619–640.

685 Cann, J.R., Blackman, D.K., Smith, D.K., McAllister, E., Janssen, B., Mello, S., Avgerinos, E., Pascoe,  
686 A.R., Escartin, J., 1997, Corrugated slip surfaces formed at ridge–transform intersections on the  
687 Mid-Atlantic Ridge: Nature, v. 385, p. 329–332.

688 Cannat, M., 1993, Emplacement of mantle rocks in the seafloor at mid-ocean ridges: Journal of  
689 Geophysical Research: Solid Earth, v. 98, p. 4163–4172.

690 Cannat M., Fontaine F., Escartin J., 2010, Serpentinization and associated hydrogen and methane fluxes  
691 at slow spreading ridges, in Rona P.A., Devey C.W., Dymont J., Murton B.J., ed. Diversity of  
692 Hydrothermal Systems on Slow Spreading Ocean Ridges, 188, American Geophysical Union,  
693 Geophysical Monograph Series, v. 188, p. 241-264, 9780875904788.

694 Charlou, J.L., Donval, J.P., Fouquet, Y., Jean-Baptiste, P., Holm, N., 2002, Geochemistry of high H<sub>2</sub> and  
695 CH<sub>4</sub> vent fluids issuing from ultramafic rocks at the Rainbow hydrothermal field (36°14'N,  
696 MAR): Chemical Geology, v. 191, p. 345–359.

697 Cherkashev, G.A., Ivanov, V.N., Bel'tenev, V.I., Lazareva, L.I., Rozhdestvenskaya, I.I., Samovarov,  
698 M.L., Poroshina, I.M., Sergeev, M.B., Stepanova, T.V., Dobretsova, I.G., Kuznetsov, V.Yu.,  
699 2013, Massive sulfide ores of the northern equatorial Mid-Atlantic Ridge: Oceanology, v. 53, p.  
700 607–619.

701 Coltat, R., Boulvais, P., Riegler, T., Pelleter, E., Branquet, Y., 2021, Element distribution in the root zone  
702 of ultramafic-hosted black smoker-like systems: Constraints from an Alpine analog: *Chemical*  
703 *Geology*, v. 559, 119916.

704 Connelly, D.P., Copley, J.T., Murton, B.J., Stansfield, K., Tyler, P.A., German, C.R., Van Dover, C.L.,  
705 Amon, D., Furlong, M., Grindlay, N. and Hayman, N., 2012, Hydrothermal vent fields and  
706 chemosynthetic biota on the world's deepest seafloor spreading centre: *Nature*  
707 *communications*, v. 3, p. 1-9.

708 Cook, N.J., Halls, C., Boyle, A.P., 1993, Deformation and metamorphism of massive sulphides at  
709 Sulitjelma, Norway: *Mineralogical Magazine*, v. 57, p. 67–81.

710 Cox, S., Fagereng, A., MacLeod, C.J., 2021, Shear zone development in serpentized mantle:  
711 implications for the strength of oceanic transform faults: *Journal of Geophysical Research: Solid*  
712 *Earth*, v. 126, p. 1-28.

713 Denny, A.R., Kelley, D.S. and Früh-Green, G.L., 2016, Geologic evolution of the Lost City hydrothermal  
714 field: *Geochemistry, Geophysics, Geosystems*, v. 17, p.375-394.

715 Deschamps, F., Godard, M., Guillot, S., Hattori, K., 2013, Geochemistry of subduction zone  
716 serpentinites: *Lithos*, v. 178, p. 96–127.

717 Dubinina, E.O., Bortnikov, N.S., Stavrova, O.O., Kossova, S.A., 2020, Sulfur Isotope Fractionation  
718 During Sulfide Generation in the Hydrothermal Submarine Systems: The Case of Logatchev,  
719 Krasnov, and Rainbow Hydrothermal Fields, Mid-Atlantic Ridge: *Geology of Ore Deposits*, v.  
720 62, p. 351–371.

721 Eckstrand, O.R., and Hulbert, L.J. 1987. Selenium and the source of sulphur in magmatic nickel and  
722 platinum deposits [abs.]: Geological Association of Canada - Mineralogical Association of  
723 Canada Annual Meeting, Program with Abstracts, 1987, v.12, p. 40.

724 Escartin, J., Mével, C., Petersen, S., Bonnemains, D., Cannat, M., Andreani, M., Augustin, N., Bezos, A.,  
725 Chavagnac, V., Choi, Y. and Godard, M., 2017. Tectonic structure, evolution, and the nature of  
726 oceanic core complexes and their detachment fault zones (13 20' N and 13 30' N, Mid Atlantic  
727 Ridge): *Geochemistry, Geophysics, Geosystems*, v.18, p.1451-1482.

728 Escartín, J., Mével, C., MacLeod, C.J., McCaig, A.M., 2003, Constraints on deformation conditions and  
729 the origin of oceanic detachments: The Mid-Atlantic Ridge core complex at 15°45'N:  
730 *Geochemistry, Geophysics, Geosystems*, v. 4(8), p.1067.

731 Fagereng, A., MacLeod, C.J., 2019, On seismicity and structural style of oceanic transform faults: a field  
732 geological perspective from the Troodos ophiolite, Cyprus, in Duarte, J.C. ed., *Transform Plate  
733 Boundaries and Fracture Zones*, Elsevier Books, p. 437-459.

734 Firstova, A., Stepanova, T., Cherkashov, G., Goncharov, A., Babaeva, S., 2016, Composition and  
735 Formation of Gabbro-Peridotite Hosted Seafloor Massive Sulfide Deposits from the Ashadze-1  
736 Hydrothermal Field, Mid-Atlantic Ridge: *Minerals*, v. 6, p. 19.

737 Foose, M.P., Economou, M., Panayiotou, A., 1985, Compositional and mineralogic constraints on the  
738 genesis of ophiolite hosted nickel mineralization in the Pevkos area, Limassol Forest, Cyprus:  
739 *Mineralium Deposita*, v. 20, p. 234–240.

740 Fornari, D.J., Gallo, D.G., Edwards, M.H., Madsen, J.A., Perfit, M.R., Shor, A.N., 1989, Structure and  
741 topography of the Siqueiros transform fault system: Evidence for the development of intra-  
742 transform spreading centers: *Marine Geophysical Researches*, v. 11, p. 263–299.

743 Fouquet, Y., Cambon, P., Etoubleau, J., Charlou, J.L., Ondréas, H., Barriga, F.J.A.S., Cherkashov, G.,  
744 Semkova, T., Poroshina, I., Bohn, M., Donval, J.P., Henry, K., Murphy, P., Rouxel, O., 2010,  
745 Geodiversity of hydrothermal processes along the Mid-Atlantic Ridge and ultramafic-hosted  
746 mineralization: A new type of oceanic Cu-Zn-Co-Au volcanogenic massive sulfide deposit, in

747 Rona, P.A., Devey, C.W., Dymant, J., Murton, B.J., ed., Geophysical Monograph Series,  
748 American Geophysical Union, Washington, D.C., p. 321–367.

749 Fouquet, Y., Charlou J. L., Ondreas H., Radford-Knoery J., Donval J.P., Douville E., Apprioual R.,  
750 Cambon P., Pelle H., Landure J.Y., Normand A., Ponzevera E., German C., Parson L., Barriga  
751 F.J.A.S., Costa I., Relvas J., Ribeiro A., 1997, Discovery and first submersible on the Rainbow  
752 hydrothermal field on the MAR (36°14'N): Eos Transactions, American Geophysical Union, 78,  
753 832.

754 Francis, T.J.G., 1981, Serpentinization faults and their role in the tectonics of slow spreading ridges:  
755 Journal of Geophysical Research: Solid Earth, v. 86, p. 11616–11622.

756 Früh-Green, G.L., Kelley, D.S., Bernasconi, S.M., Karson, J.A., Ludwig, K.A., Butterfield, D.A., Boschi,  
757 C., Proskurowski, G., 2003, 30,000 Years of Hydrothermal Activity at the Lost City Vent Field:  
758 Science v. 301, p. 495–498.

759 Gale, A., Dalton, C.A., Langmuir, C.H., Su, Y., Schilling, J.-G., 2013, The mean composition of ocean  
760 ridge basalts. *Geochemistry, Geophysics, Geosystems*, v. 14, p. 489–518.

761 Gass, I.G., 1968. Is the Troodos Massif of Cyprus a Fragment of Mesozoic Ocean Floor? *Nature*, v. 220,  
762 p. 39–42.

763 Gass, I. G., 1980, The Troodos Massif: Its Role in the Unravelling of the Ophiolite Problem and Its  
764 Significance in the Understanding of Constructive Plate Margin Processes, in Malpas J., Moores,  
765 E.M., Panayiotou, A. & Xenophontos, C., ed., *Ophiolites: Ocean Crustal Analogues*.  
766 Proceedings of the International Ophiolite Symposium 1979, Geological Survey Department of  
767 Cyprus, Nicosia, Cyprus, pp. 23–35.

768 Gass I.G. MacLeod C.J. Murton B.J. Panayiotou A. Simonian K.O. Xenophontos C., 1994, The Geology  
769 of the Southern Troodos Transform Fault Zone: Nicosia, Cyprus, Geological Survey Department  
770 Cyprus, Ministry of Agriculture, Natural Resources and Environment, Memoir 9, p. 218.



- 771 Gülaçar, O.F., Delaloye, M., 1976, Geochemistry of nickel, cobalt and copper in alpine-type ultramafic  
772 rocks: *Chemical Geology*, v. 17, p. 269–280.
- 773 Hannington, M.D., de Ronde, C.D.J., Petersen, S., 2005, Sea-floor tectonics and submarine hydrothermal  
774 systems, in Hedenquist, J.W., Thompson, J.F.H., Goldfarb, R.J., Richards, J.P. ed., *Economic  
775 Geology 100th Anniversary Volume*. Society of Economic Geologists, Littelton, Colorado, USA,  
776 p. 111–141.
- 777 Hannington, M.D., Bleeker, W., Kjarsgaard, I., 1999, Sulfide Mineralogy, Geochemistry, and Ore  
778 Genesis of the Kidd Creek Deposit: Part II. The Bornite Zone\*, in: Hannington, Mark D., Barrie,  
779 C.T. ed., *The Giant Kidd Creek Volcanogenic Massive Sulfide Deposit, Western Abitibi  
780 Subprovince, Canada*. Society of Economic Geologists, p. 225 - 266
- 781 Harris, D.C., Nickel, E.H., 1972, Pentlandite compositions and associations in some mineral deposits:  
782 *Canadian Mineralogist*, v. 11, p. 861–878.
- 783 Hekinian, R., Bideau, D., Cannat, M., Francheteau, J., Hébert, R., 1992, Volcanic activity and crust-  
784 mantle exposure in the ultrafast Garrett transform fault near 13°28'S in the Pacific: *Earth and  
785 Planetary Science Letters*, v. 108, p. 259–275.
- 786 Huber, H., Koeberl, C., McDonald, I., Reimold, W.U., 2001, Geochemistry and petrology of  
787 Witwatersrand and Dwyka diamictites from South Africa: search for an extraterrestrial  
788 component: *Geochimica et Cosmochimica Acta*, v. 65, p. 2007–2016.
- 789 Huston, D.L., Sie, S.H., Suter, G.F., 1995, Selenium and its importance to the study of ore genesis: the  
790 theoretical basis and its application to volcanic-hosted massive sulfide deposits using PIXE  
791 analysis: *Nuclear Instruments and Methods in Physics Research Section B: Beam Interactions  
792 with Materials and Atoms, Nuclear Microprobe Technology and Applications*, v. 104, p.476–480.

793 Ildefonse, B., Blackman, D.K., John, B.E., Ohara, Y., Miller, D.J., MacLeod, C.J., Integrated Ocean  
794 Drilling Program Expeditions 304/305 Science Party, 2007, Oceanic core complexes and crustal  
795 accretion at slow-spreading ridges: *Geology*, v. 35, p. 623–626.

796 Jowitt, S.M., Jenkin, G.R.T., Coogan, L.A., Naden, J., 2012, Quantifying the release of base metals from  
797 source rocks for volcanogenic massive sulfide deposits: Effects of protolith composition and  
798 alteration mineralogy: *Journal of Geochemical Exploration*, v. 118, p. 47–59.

799 Kampschulte, A., Strauss, H., 2004, The sulfur isotopic evolution of Phanerozoic seawater based on the  
800 analysis of structurally substituted sulfate in carbonates: *Chemical Geology*, v. 204, p. 255–286.

801 Keith, M., Haase, K.M., Klemd, R., Krumm, S., Strauss, H., 2016, Systematic variations of trace element  
802 and sulfur isotope compositions in pyrite with stratigraphic depth in the Skouriotissa volcanic-  
803 hosted massive sulfide deposit, Troodos ophiolite, Cyprus: *Chemical Geology*, v. 423, p. 7–18.

804 Kelley, D.S., Karson, J.A., Blackman, D.K., Früh-Green, G.L., Butterfield, D.A., Lilley, M.D., Olson,  
805 E.J., Schrenk, M.O., Roe, K.K., Lebon, G.T., Rivizzigno, P., 2001, An off-axis hydrothermal vent  
806 field near the Mid-Atlantic Ridge at 30° N: *Nature*, v. 412, p. 145–149.

807 Klein, F., Bach, W., 2009, Fe–Ni–Co–O–S Phase Relations in Peridotite–Seawater Interactions: *Journal*  
808 *of Petrology*, v. 50, p. 37–59.

809 Krasnov, S.G., Cherkashev, G.A., Stepanova, T.V., Batuyev, B.N., Krotov, A.G., Malin, B.V., Maslov,  
810 M.N., Markov, V.F., Poroshina, I.M., Samovarov, M.S., Ashadze, A.M., Lazareva, L.I.,  
811 Ermolayev, I.K., 1995, Detailed geological studies of hydrothermal fields in the North Atlantic:  
812 *Geological Society, London Special Publication*, v. 87, p. 43–64.

813 Lafrance, B., Gibson, H.L., Stewart, M.S., 2020, Chapter 4: Internal and External Deformation and  
814 Modification of Volcanogenic Massive Sulfide Deposits, in Rowland J.V., Rhys D.A. ed.,  
815 *Applied Structural Geology of ore-forming hydrothermal systems*, Society of Economic  
816 Geologists, *Reviews in Economic Geology*, v.21, pp. 147-171.

- 817 Layton-Matthews, D., Leybourne, M.I., Peter, J.M., Scott, S.D., Cousens, B., Eglington, B.M., 2013,  
818 Multiple sources of selenium in ancient seafloor hydrothermal systems: Compositional and Se, S,  
819 and Pb isotopic evidence from volcanic-hosted and volcanic-sediment-hosted massive sulfide  
820 deposits of the Finlayson Lake District, Yukon, Canada: *Geochimica et Cosmochimica Acta*, v.  
821 117, p. 313–331.
- 822 Leblanc, M., Billaud, P., 1982, Cobalt arsenide orebodies related to an upper Proterozoic ophiolite; Bou  
823 Azzer (Morocco): *Economic Geology*, v. 77, p. 162–175.
- 824 Lein Yu.A., Ulyanova N.V., Ulyanov A.A., Cherkashev G.A., Stepanova T.V., 2001, Mineralogy and  
825 geochemistry of sulfide ores in ocean-floor hydrothermal fields associated with serpentinite  
826 protrusions: *Russian Journal of Earth Science*, v. 3, p. 371-393
- 827 Liu, W., Borg, S.J., Testemale, D., Etschmann, B., Hazemann, J.-L., Brugger, J., 2011, Speciation and  
828 thermodynamic properties for cobalt chloride complexes in hydrothermal fluids at 35–440°C and  
829 600bar: An in-situ XAS study: *Geochimica et Cosmochimica Acta*, v. 75, p. 1227–1248.
- 830 Liu, W., Migdisov, A., Williams-Jones, A., 2012, The stability of aqueous nickel(II) chloride complexes  
831 in hydrothermal solutions: Results of UV–Visible spectroscopic experiments: *Geochimica et*  
832 *Cosmochimica Acta*, v. 94, p. 276–290.
- 833 Lode, S., Piercey, S.J., Layne, G.D., Piercey, G., Cloutier, J., 2017, Multiple sulphur and lead sources  
834 recorded in hydrothermal exhalites associated with the Lemarchant volcanogenic massive  
835 sulphide deposit, central Newfoundland, Canada: *Mineralium Deposita*, v. 52, p. 105-128.
- 836 MacDonald, A.H., Fyfe, W.S., 1985, Rate of serpentinization in seafloor environments: *Tectonophysics*,  
837 *Oceanic Lithosphere*, v. 116, p. 123–135.
- 838 Machel, H.G., Krouse, H.R., Sassen, R., 1995, Products and distinguishing criteria of bacterial and  
839 thermochemical sulfate reduction: *Applied Geochemistry*, v. 10, p. 373–389.

840 MacLeod, C.J., 1988, The Tectonic Evolution of the Eastern Limassol Forest Complex, Cyprus: Ph.D.  
841 Thesis, Milton Keynes, UK, The Open University, p. 368.

842 MacLeod, C.J., 1990, Role of the Southern Troodos Transform Fault in the rotation of the Cyprus  
843 microplate: evidence from the Eastern Limassol Forest Complex. In: Malpas J., Moores, E.M.,  
844 Panayiotou, A. & Xenophontos, C., ed., Ophiolites: Ocean Crustal Analogues. Proceedings of  
845 the Symposium Troodos 1987, Geological Survey Department, Nicosia, Cyprus, p.75-85.

846 MacLeod, C.J., Allerton, S., Gass, I.G., Xenophontos, C., 1990, Structure of a fossil ridge–transform  
847 intersection in the Troodos ophiolite: *Nature*, v. 348, p. 717–720.

848 MacLeod, C.J., Escartín, J., Banerji, D., Banks, G.J., Gleeson, M., Irving, D.H.B., Lilly, R.M., McCaig,  
849 A.M., Niu, Y., Allerton, S., Smith, D.K., 2002, Direct geological evidence for oceanic  
850 detachment faulting: The Mid-Atlantic Ridge, 15°45'N: *Geology*, v. 30, p. 879–882.

851 MacLeod, C.J., Murton, B.J., 1993, Structure and tectonic evolution of the Southern Troodos Transform  
852 Fault Zone, Cyprus. Geological Society of London Special Publication, v. 76, p. 141–176.

853 MacLeod, C., Murton, B., 1995, On the sense of slip of the Southern Troodos Transform-Fault Zone,  
854 Cyprus: *Geology*, v. 23, p. 257-260.

855 Marques, A.F.A., Barriga, F., Chavagnac, V., Fouquet, Y., 2006. Mineralogy, geochemistry, and Nd  
856 isotope composition of the Rainbow hydrothermal field, Mid-Atlantic Ridge: *Mineralium*  
857 *Deposita*, v. 41, p. 52-67.

858 Marshall, B., Gilligan, L., 1987, An introduction to remobilization: Information from ore-body geometry  
859 and experimental considerations: *Ore Geology Reviews* v. 2, p. 87–131.

860 Martin, A.J., Keith, M., McDonald, I., Haase, K.M., McFall, K.A., Klemd, R., MacLeod, C.J., 2019,  
861 Trace element systematics and ore-forming processes in mafic VMS deposits: Evidence from the  
862 Troodos ophiolite, Cyprus: *Ore Geology Reviews*, v. 106, p. 205–225.

863 Martin, A.J., Keith, M., Parvaz, D.B., McDonald, I., Boyce, A.J., McFall, K.A., Jenkin, G.R.T., Strauss,  
864 H., MacLeod, C.J., 2020, Effects of magmatic volatile influx in mafic VMS hydrothermal  
865 systems: Evidence from the Troodos ophiolite, Cyprus: *Chemical Geology*, v. 531, 119325.

866 Martin, A.J., McDonald, I., Jenkin, G.R.T., McFall, K.A., Boyce, A.J., Jamieson, J.W., MacLeod, C.J.,  
867 2021, A missing link between ancient and active mafic-hosted seafloor hydrothermal systems –  
868 Magmatic volatile influx in the exceptionally preserved Mala VMS deposit, Troodos, Cyprus.  
869 *Chemical Geology*, v. 567, 120127.

870 McCaig, A.M., Cliff, B., Escartín, J., Fallick, A.E., MacLeod, C.J., 2007, Oceanic detachment faults  
871 focus very large volumes of black smoker fluids: *Geology*, v. 35, p. 935-938.

872 McDonald, I., Viljoen, K.S., 2006, Platinum-group element geochemistry of mantle eclogites: a  
873 reconnaissance study of xenoliths from the Orapa kimberlite, Botswana: *Applied Earth Science*,  
874 v. 115, p. 81–93.

875 Melekestseva, I., Maslennikov, V., Tret'yakov, G., Maslennikova, S., Danyushevsky, L., Kotlyarov, V.,  
876 Large, R., Beltenev, V., Khvorov, P., 2020, Trace Element Geochemistry of Sulfides from the  
877 Ashadze-2 Hydrothermal Field (12°58' N, Mid-Atlantic Ridge): Influence of Host Rocks,  
878 Formation Conditions or Seawater? *Minerals*, v. 10, p. 743.

879 Melekestseva, I.Yu., Tret'yakov, G.A., Nimis, P., Yuminov, A.M., Maslennikov, V.V., Maslennikova,  
880 S.P., Kotlyarov, V.A., Beltenev, V.E., Danyushevsky, L.V., Large, R., 2014, Barite-rich massive  
881 sulfides from the Semenov-1 hydrothermal field (Mid-Atlantic Ridge, 13°30.87' N): Evidence for  
882 phase separation and magmatic input: *Marine Geology*, v. 349, p. 37–54.

883 Mével, C., 2003. Serpentinization of abyssal peridotites at mid-ocean ridges. *Comptes Rendus*  
884 *Geoscience*, v. 335, p. 825–852.

885 Miyashiro, A., 1973, The Troodos ophiolitic complex was probably formed in an island arc, Earth and  
886 Planetary Science Letters, v. 19, p. 218–224.

887 Moody, J.B., 1976, Serpentinization: a review: Lithos, v. 9, p.125-138.

888 Moores, E.M., Vine, F.J., Gast, P.W., Bullard, E.C., Cann, J.R., Matthews, D.H., 1971, The Troodos  
889 Massif, Cyprus and other ophiolites as oceanic crust: evaluation and implications: Philosophical  
890 Transactions of the Royal Society of London Mathematics and Physical Sciences, v. 268, p. 443–  
891 467.

892 Mukasa, S.B., Ludden, J.N., 1987, Uranium-lead isotopic ages of plagiogranites from the Troodos  
893 ophiolite, Cyprus, and their tectonic significance: Geology, v. 15, p. 825–828.

894 Murton, B.J., 1986a, Anomalous oceanic lithosphere formed in a leaky transform fault: evidence from the  
895 Western Limassol Forest Complex, Cyprus: Journal of the Geological Society, v. 143, p. 845–  
896 854.

897 Murton, B.J., 1986b, Tectonic evolution of the Western Limassol Forest Complex, Cyprus: Ph.D Thesis,  
898 Milton Keynes, UK, The Open University, p. 198.

899 Naldrett, A.J., Duke, J.M., 1980, Platinum metals magmatic sulfide ores: Science, v. 208, p. 1417–1424.

900 Naldrett, A.J., Hoffman, E.L., Green, A.H., Chou, C.L., Naldrett, S.R., Alcock, R.A., 1979, The  
901 composition of Ni-sulfide ores, with particular reference to their content of PGE and Au:  
902 Canadian Mineralogist, v. 17, p. 403–415.

903 Ohmoto H., Rye R.O., 1979, Isotopes of sulfur and carbon. In: Geochemistry of Hydrothermal Ore  
904 Deposits, in Barnes, H.L., ed., Geochemistry of hydrothermal ore deposit, 3<sup>rd</sup> edition: New York,  
905 John Wiley and Sones, Inc., p. 509-567.

906 Ono, S., Keller, N.S., Rouxel, O., Alt, J.C., 2012, Sulfur-33 constraints on the origin of secondary pyrite  
907 in altered oceanic basement: Geochimica et Cosmochima Acta, v. 87, p. 323–340.

908 Palme, H. and O'Neill, H.S.C., 2003, Cosmochemical estimates of mantle composition in Carlson R.W.,  
909 ed., *Treatise in geochemistry*, Vol. 2, The mantle and core pp.1-38. Oxford: Elsevier-Pergamon

910 Palandri, J.L., Reed, M.H., 2004. Geochemical models of metasomatism in ultramafic systems:  
911 serpentinization, rodingitization, and sea floor carbonate chimney precipitation: *Geochimica et*  
912 *Cosmochimica Acta*, v. 68, p. 1115–1133.

913 Panayiotou, A., 1980, Cu-Ni-Co-Fe sulphide mineralization, Limassol Forest, Cyprus, in Malpas J.,  
914 Moores, E.M., Panayiotou, A. & Xenophontos, C., ed., *Ophiolites: Ocean Crustal Analogues*.  
915 *Proceedings of the International Ophiolite Symposium 1979*, Geological Survey Department of  
916 Cyprus, Nicosia, Cyprus, p. 102-116.

917 Parkkinen, J., Loukola-Ruskeeniemi, K. and Sorjonen-Ward, P., 1997, An outline of the history of  
918 exploration and mining in the Outokumpu district: Research and exploration — where do they  
919 meet? 4th Biennial SGA Meeting, August 11–13, 1997, Turku, Finland. Excursion guidebook  
920 A4, Geological Survey of Finland, Guide, v. 42, p. 27-28.

921 Patten, C.G.C., Coltat, R., Junge, M., Peillod, A., Ulrich, M., Manatschal, G., Kolb, J., 2022, Ultramafic-  
922 hosted volcanogenic massive sulfide deposits: an overlooked sub-class of VMS deposit forming  
923 in complex tectonic environments: *Earth-Science Reviews* v. 224, 103891.

924 Pearce, J.A., 1975. Basalt geochemistry used to investigate past tectonic environments on Cyprus:  
925 *Tectonophysics*, v. 25, p. 41–67.

926 Pearce, J.A., Robinson, P.T., 2010, The Troodos ophiolitic complex probably formed in a subduction  
927 initiation, slab edge setting: *Gondwana Research*, v. 18, p. 60–81.

928 Peltonen, P., Kontinen, A., Huhma, H., Kuronen, U., 2008, Outokumpu revisited: New mineral deposit  
929 model for the mantle peridotite-associated Cu–Co–Zn–Ni–Ag–Au sulphide deposits: *Ore*  
930 *Geology Reviews*, v. 33, p. 559–617.

931 Petersen, S., Kuhn, K., Kuhn, T., Augustin, N., Hékinian, R., Franz, L., Borowski, C., 2009, The  
932 geological setting of the ultramafic-hosted Logatchev hydrothermal field (14°45'N, Mid-Atlantic  
933 Ridge) and its influence on massive sulfide formation: *Lithos*, v. 112, p. 40–56.

934 Prichard, H.M., Knight, R.D., Fisher, P.C., McDonald, I., Zhou, M.-F., Wang, C.Y., 2013, Distribution of  
935 platinum-group elements in magmatic and altered ores in the Jinchuan intrusion, China: an  
936 example of selenium remobilization by postmagmatic fluids: *Mineralium Deposita*, v. 48, p. 767–  
937 786.

938 Prichard, H.M., Lord, R.A., 1990, Platinum and palladium in the Troodos ophiolite complex, Cyprus:  
939 *Canadian Mineralogist*, v. 28, p. 607–617.

940 Queffurus, M., Barnes, S.-J., 2015, A review of sulfur to selenium ratios in magmatic nickel–copper and  
941 platinum-group element deposits: *Ore Geology Reviews*, v. 69, p. 301–324.

942 Robertson, A.H.F., 1977, Tertiary uplift history of the Troodos massif, Cyprus: *Geological Society of  
943 America Bulletin*, v. 88, p. 1763–1772.

944 Rona, P.A., Widenfalk, L., Boström, K., 1987. Serpentinized ultramafics and hydrothermal activity at the  
945 Mid-Atlantic Ridge crest near 15°N: *Journal of Geophysical Research: Solid Earth*, v. 92, p.  
946 1417–1427.

947 Rouxel, O., Fouquet, Y., Ludden, J.N., 2004, Copper Isotope Systematics of the Lucky Strike, Rainbow,  
948 and Logatchev Sea-Floor Hydrothermal Fields on the Mid-Atlantic Ridge: *Economic Geology*, v.  
949 99, p. 585–600.

950 Sakai, H., 1968, Isotopic properties of sulfur compounds in hydrothermal processes: *Geochemical  
951 Journal*, v. 2, p. 29–49.

952 Seyfried, W.E., Mottl, M.J., 1982, Hydrothermal alteration of basalt by seawater under seawater-  
953 dominated conditions. *Geochimica et Cosmochimica Acta*, v. 46, p. 985–1002.



954 Simonian, K.O., 1975. The Geology of the Arakapas Fault Belt Area Troodos Massif, Cyprus: Ph.D  
955 thesis, Milton Keynes, UK, The Open University, pp. 151.

956 Simonian, K.O., Gass, I.G., 1978, Arakapas fault belt, Cyprus: A fossil transform fault. Geological  
957 Society of American Bulletin, v. 89, p. 1220–1230.

958 Smith, J.W., Holwell, D.A., McDonald, I., Boyce, A.J., 2016, The application of S isotopes and S/Se  
959 ratios in determining ore-forming processes of magmatic Ni–Cu–PGE sulfide deposits: A  
960 cautionary case study from the northern Bushveld Complex: Ore Geology Reviews, v. 73, p. 148–  
961 174.

962 Takai, K., Nakamura, K., Toki, T., Tsunogai, U., Miyazaki, M., Miyazaki, J., Hirayama, H., Nakagawa,  
963 S., Nunoura, T., Horikoshi, K., 2008, Cell proliferation at 122°C and isotopically heavy CH<sub>4</sub>  
964 production by a hyperthermophilic methanogen under high-pressure cultivation: Proceedings of  
965 the National Academy of Sciences of the United States of America, v. 105, p. 10949–10954.

966 Tao, C., Seyfried, W.E., Lowell, R.P., Liu, Y., Liang, J., Guo, Z., Ding, K., Zhang, H., Liu, J., Qiu, L.,  
967 Egorov, I., Liao, S., Zhao, M., Zhou, J., Deng, X., Li, H., Wang, H., Cai, W., Zhang, G., Zhou,  
968 H., Lin, J., Li, W., 2020, Deep high-temperature hydrothermal circulation in a detachment  
969 faulting system on the ultra-slow spreading ridge: Nature Communications, v. 11, 1300.

970 Thalhammer, O., Stumpfl, E.F., Panayiotou, A., 1986, Postmagmatic, hydrothermal origin of sulfide and  
971 arsenide mineralizations at Limassol Forest, Cyprus: Mineralium Deposita, v. 21, p. 95–105.

972 Wang, Y., Han, X., Petersen, S., Frische, M., Qiu, Z., Cai, Y., Zhou, P., 2018, Trace Metal Distribution in  
973 Sulfide Minerals from Ultramafic-Hosted Hydrothermal Systems: Examples from the Kairei Vent  
974 Field, Central Indian Ridge: Minerals, v. 8, 526.

975 Yamamoto, M., 1976, Relationship between Se/S and sulfur isotope ratios of hydrothermal sulfide  
976 minerals: Mineralium Deposita, v. 11, p. 197–209.

977 **Figure Captions**

978 Figure 1: Location map of Lakxia tou Mavrou and surrounding area. A) Location of the Southern Troodos  
979 Transform Fault Zone (STTFZ) on the island of Cyprus. B) Geological map of the STTFZ (delineated by  
980 the two dashed white lines) with major geological terranes that form the STTFZ highlighted (AFB =  
981 Arakapas Fault Belt, LFC= Limassol Forest Complex). C) The location of Lakxia tou Mavrou. D) Map  
982 showing the location of the sulfide mineralization at Lakxia tou Mavrou (after BMG, 2015). Coordinates  
983 in WGS 1984, Zone 36S.

984 Figure 2: Field photographs from Lakxia tou Mavrou. A) Sheared Transform Sequence dyke containing  
985 sulfide blebs (inset image). B) Sheared and boudinaged transform sequence dyke in serpentinite (arrows  
986 indicate shear sense). C) Serpentinite fabric showing dextral slip kinematics (E-W lineation) from the  
987 serpentinite shear zone. D) Contact between massive pyrrhotite and serpentinite in the historic adit (see Fig.  
988 1B). E and F) Vein mineralization with a mesh of pyrrhotite, isocubanite and chalcopyrite (gray-yellow) in  
989 serpentinite (green-white) with a mylonitic texture. F\*) Inset image showing close-up view of serpentinite  
990 (Serp.) clasts and sheared mylonitic sulfides. Red lines show serpeninite clasts with a crude sigmoidal  
991 shape. G) Massive pyrrhotite with disseminated chalcopyrite and Co-pentlandite from the exposed gossan.

992 Figure 3: Photomicrographs in reflected light of massive sulfide samples. A) Magnetite-bearing breccia  
993 zone in pyrrhotite. B) Ductile deformation in pyrrhotite exhibiting a “fingerprint” texture with minor  
994 magnetite. C) Chalcopyrite with lamella of isocubanite and pyrrhotite. D) Euhedral chrome spinel grain in  
995 pyrrhotite with pitting and alteration at the grain margin. Minor magnetite. E) False color element map of  
996 a massive sulfide sample. Disseminated Co-pentlandite is clearly visible as orange grains in pyrrhotite.  
997 Magnetite-bearing breccia zones with silicate material occur cross-cutting the sample. Cp = chalcopyrite  
998 (blue-purple in E), Po = pyrrhotite (pink), Crs = chrome spinel (green), Icb = isocubanite (not visible in E),  
999 Mag = magnetite (red-brown), Si = silica (green-brown).

1000 Figure 4: Photomicrographs in reflected light of veined samples. A) Isocubanite associated with  
1001 chalcopyrite, pyrrhotite and Co-pentlandite. B) Massive pyrrhotite and isocubanite with interstitial  
1002 chalcopyrite. Co-pentlandite is associated with pyrrhotite. C) Euhedral chrome spinel surrounded by  
1003 chalcopyrite, cubanite and minor pyrrhotite. D) Chrome spinel with a pitted appearance and a lighter  
1004 colored alteration rim of ferri-chromite. E) Isocubanite being replaced by chalcopyrite at the contact with  
1005 surrounding serpentinite. F) Chalcopyrite exsolution in isocubanite. G) Massive pyrrhotite. H) Close up  
1006 image of feathery inclusions of Co-pentlandite in pyrrhotite. I) Chalcopyrite at the contact between  
1007 pyrrhotite and serpentinite brecciated vein. J) Mesh textured veins of chalcopyrite and pyrrhotite. K)  
1008 Serpentinite veins in pyrrhotite. L) Brittle deformation where individual sulfide grains appear fragmented.  
1009 Po = pyrrhotite, Icb = isocubanite, Co-Pn = cobalt pentlandite, Cp = chalcopyrite, CrS = chrome spinel, Srp  
1010 = serpentinite.

1011 Figure 5: False color element maps of veined samples highlighting mineralogical and textural associations.  
1012 A) Spatial association between pyrrhotite and pentlandite. Isocubanite has a massive texture whilst  
1013 chalcopyrite occurs primarily as veins. Chrome spinel is associated with serpentinite. B) Development of a  
1014 stockwork texture with a mesh of serpentinite veins. In contrast to image A, chalcopyrite occurs as  
1015 aggregates of euhedral grains within massive isocubanite. C) Chalcopyrite localized along shear bands that  
1016 cut isocubanite and pyrrhotite. Note crude sigmoidal shape to serpentinite “clasts”. Po = pyrrhotite, Icb =  
1017 isocubanite, Co-Pn = cobalt pentlandite, Cp = chalcopyrite, CrS = chrome spinel, Srp = serpentinite.

1018 Figure 6: Transform Sequence boninite dyke. A) Image in reflected light of a sulfide globule containing  
1019 chalcopyrite, pyrrhotite and chrome spinel. B) Sulfide globule in reflected light containing pyrrhotite. C)  
1020 False color element map showing micro-inclusions of pentlandite (inset image) and an alteration halo. D)  
1021 Alteration halo surrounding pyrrhotite with chromite in silicate groundmass. Pn = pentlandite, Cp =  
1022 chalcopyrite, Po = pyrrhotite, CrS = chrome spinel.

1023 Figure 7: Trace element geochemistry analyzed via LA-ICP-MS ( $n=185$  spots) for isocubanite,  
1024 chalcopyrite, pentlandite and pyrrhotite. A) Se, B) Te, C) Bi, D) Ni, E) Cu and F) Co. G) Co vs Ni. H) Zn

1025 vs. Cd. Full data in Appendix Table A1. Lower box (black) = 75<sup>th</sup> percentile, upper box (color) = 25<sup>th</sup>  
1026 percentile, median = black line, whiskers = min and max value.

1027 Figure 8: Sulfur isotope composition ( $\delta^{34}\text{S}$ ) analyzed via SIMS in pyrrhotite and chalcopyrite. Dyke-hosted  
1028 pyrrhotite is notably enriched in  $^{34}\text{S}$  relative to pyrrhotite at Lakxia tou Mavrou. Star = average, black line  
1029 = median, lower box = 75<sup>th</sup> percentile, upper box = 25<sup>th</sup> percentile, whiskers = min and max value. Note  
1030 varying Y-axis for dyke-hosted pyrrhotite.

1031 Figure 9: Chondrite normalized PGE plots. Red/blue/purple lines are data collected in this study for  
1032 massive, veined samples and dyke samples. Gray regions represent Troodos magmatic rocks.  
1033 Mineralization at Lakxia tou Mavrou is enriched in Au relative to Troodos igneous rocks (Troodos: Prichard  
1034 and Lord, 1990; chondrite values Naldrett and Duke 1980).

1035 Figure 10: Cobalt/Ni ratios from the LA-ICP-MS analysis of pyrrhotite at Lakxia tou Mavrou and pyrite at  
1036 the Skouriotissa VMS deposit (Martin et al., 2019). The median Co/Ni for harzburgite is 0.05 (\*Gulaqar  
1037 and Delaloye, 1976 and Deschamps 2013) whilst the sheeted dyke complex is 2 (\*\* Jowitt et al., 2012).  
1038 Lakxia tou Mavrou has lower Co/Ni ratios compared with Skouriotissa indicating an additional ultramafic  
1039 source of these metals at Lakxia tou Mavrou.

1040 Figure 11: Sulfur isotope composition ( $\delta^{34}\text{S}$ ) of sulfide minerals in ultramafic-hosted SMS deposits,  
1041 Troodos VMS deposits, the basalt-hosted Mala VMS deposit (Troodos) and Lakxia tou Mavrou. TO =  
1042 Troodos Ophiolite (data: Martin et al., 2021, 2020; Rouxel et al., 2004; Bogdanov et al., 1997, 2002; Lein  
1043 et al., 2001, Melekestseva 2014; Firstova et al., 2016). Max = upper quartile (UQ) + 1.5\* inter quartile  
1044 range (IQR), Min = lower quartile (LQ) – 1.5\* IQR.

1045 Figure 12: Schematic summary of sulfur isotope systematics at Lakxia tou Mavrou (not to scale). A)  
1046 Seawater precipitates anhydrite when the temperature of the hydrothermal fluid is >150°C. B) Remaining  
1047 sulfate in the fluid is transported to deeper crustal levels and, at temperatures >250°C, undergoes TSR  
1048 forming H<sub>2</sub>S. Sulfide minerals form when a small proportion of sulfate undergoes TSR (low *f* values ~0.1;

1049 after Dubinina et al., 2020). The remaining sulfate in the fluid is enriched in  $^{34}\text{S}$  relative to seawater sulfate  
1050 (~18-19‰; Kampschulte and Strauss, 2004). C) Progressive TSR continues along a fluid flow pathway,  
1051 forming sulfide minerals with progressively higher sulfur isotope values at high  $f$  values (~0.9) preserved  
1052 in sulfide blebs (not to scale) from cross-cutting dykes.

1053 Figure 13: Summary schematic for the formation of mineralization at Lakxia tou Mavrou. T1: Seawater  
1054 penetrates deep into the crust (~3-4 km) along vertical serpentinite shear zones causing the serpentinitization  
1055 of mantle peridotites releasing Ni and Co. There is insufficient heat production to drive high-temperature  
1056 hydrothermal circulation (>200 °C). T2: Intrusion of Transform Sequence plutons and early dyke swarms  
1057 in the vicinity of Lakxia tou Mavrou producing widespread high-temperature (200-500°C) hydrothermal  
1058 circulation. Anhydrite precipitates at temperatures >150°C and TSR occurs at temperatures >250°C. Where  
1059 high-temperature metal-rich fluids mix with seawater-derived fluids along E-W shear zone an initial high-  
1060 temperature sulfide mineral assemblage of pyrrhotite and Co-pentlandite forms. Mesh textured pyrrhotite  
1061 is common. Metals are leached from the margin of fractured gabbro intrusions and early dyke generations  
1062 (inset image B). T3: Transform Sequence dyke intrusion. Dykes cross-cut both serpentinitized harzburgite  
1063 and gabbros. Dyke intrusion provides a renewed influx of heat driving lower temperature hydrothermal  
1064 fluid circulation (200-300°C). Dykes provide an additional source of metals such as Cu forming an initial  
1065 isocubanite-rich mineral assemblage that is then later overprinted by chalcopyrite. Chromite is altered to  
1066 ferrichromite at its margins. Magmatic sulfide blebs are replaced by secondary pyrrhotite and chalcopyrite  
1067 where sulfur is primarily sourced by the complete TSR of seawater (high  $f$  values) forming sulfide minerals  
1068 that are enriched in  $^{34}\text{S}$  up to 20.9‰ (inset image C).

## 1069 Table Captions

1070  
1071 Table 1: Summary of LA-ICP-MS data at Lakxia tou Mavrou for pyrrhotite, chalcopyrite, cubanite, Co-  
1072 pentlandite and dyke-hosted pyrrhotite. Av = average, Med = median,  $\sigma$  = standard deviation, - = all

1073 analyses were below the detection limit. Values below detection limit are taken as half the detection limit.

1074 See Appendix A1.

1075 Table 2: Platinum Group Element data from Ni fire assay for massive, veined and dyke material at Lakxia

1076 tou Mavrou. See Appendix 2.

1077

1078

1079

1080

1081

1082

1083

1084

1085

1086

1087

1088

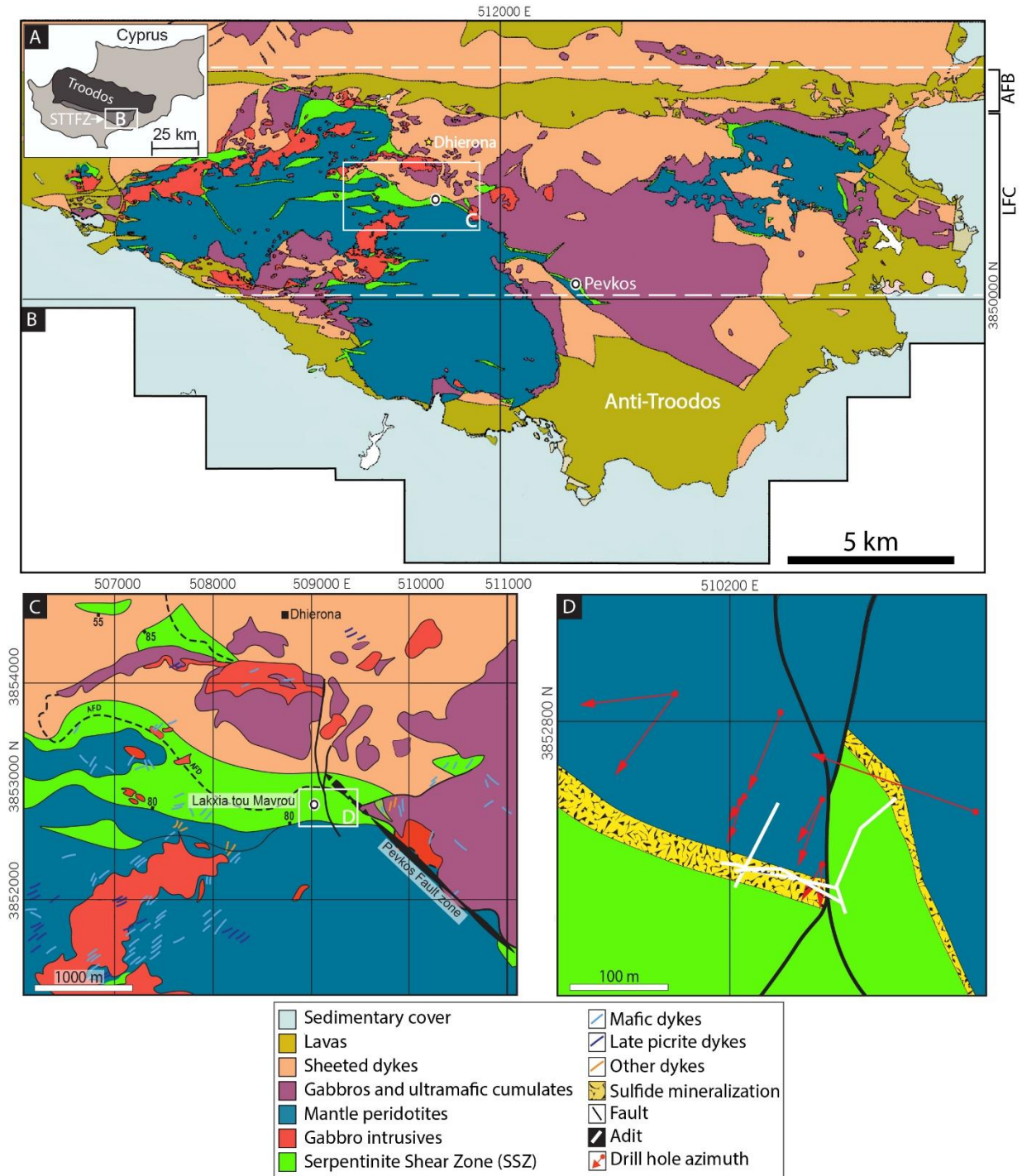
1089

1090

1091

1092

1093 Figure 1:



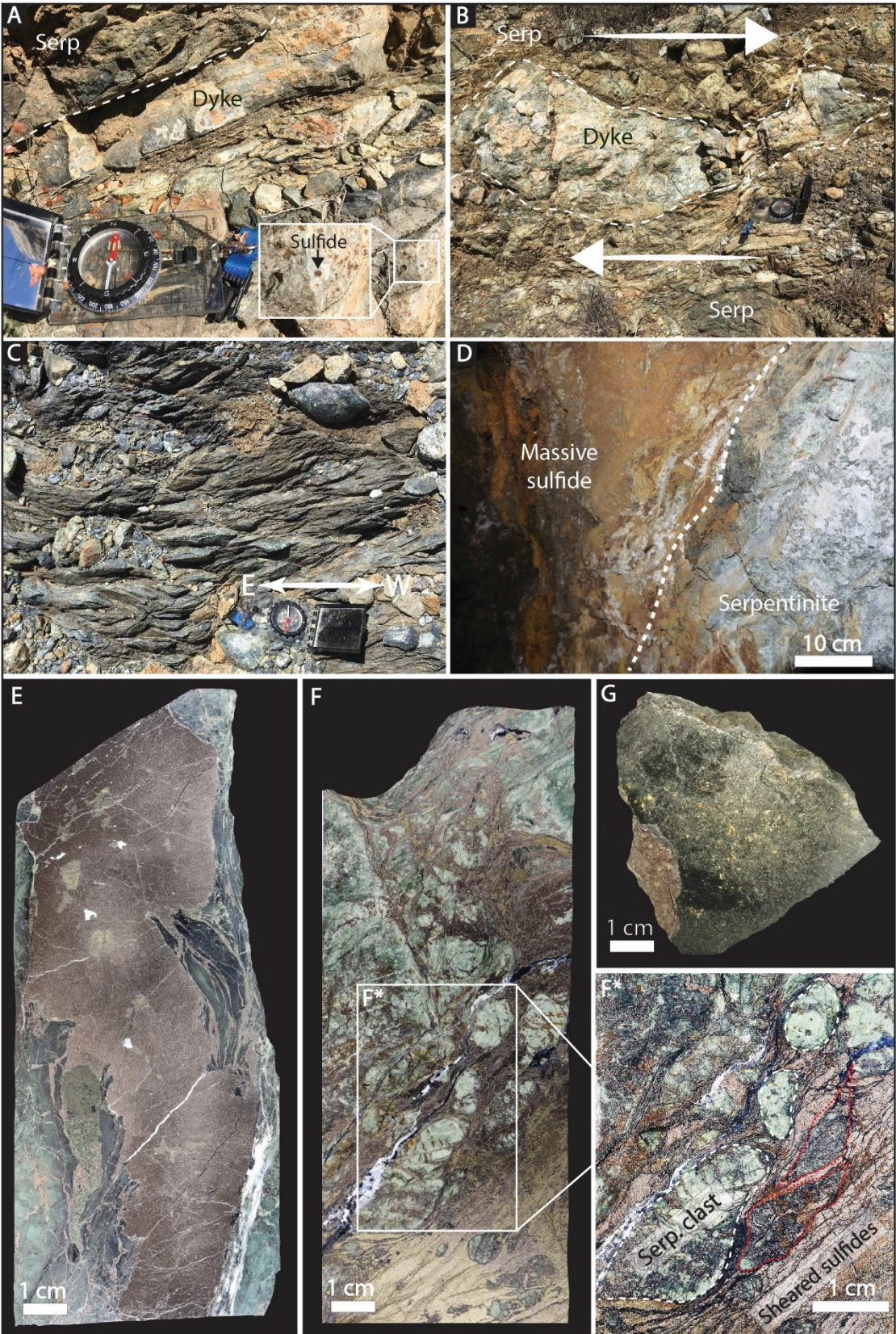
1094

1095

1096

1097 Figure 2:

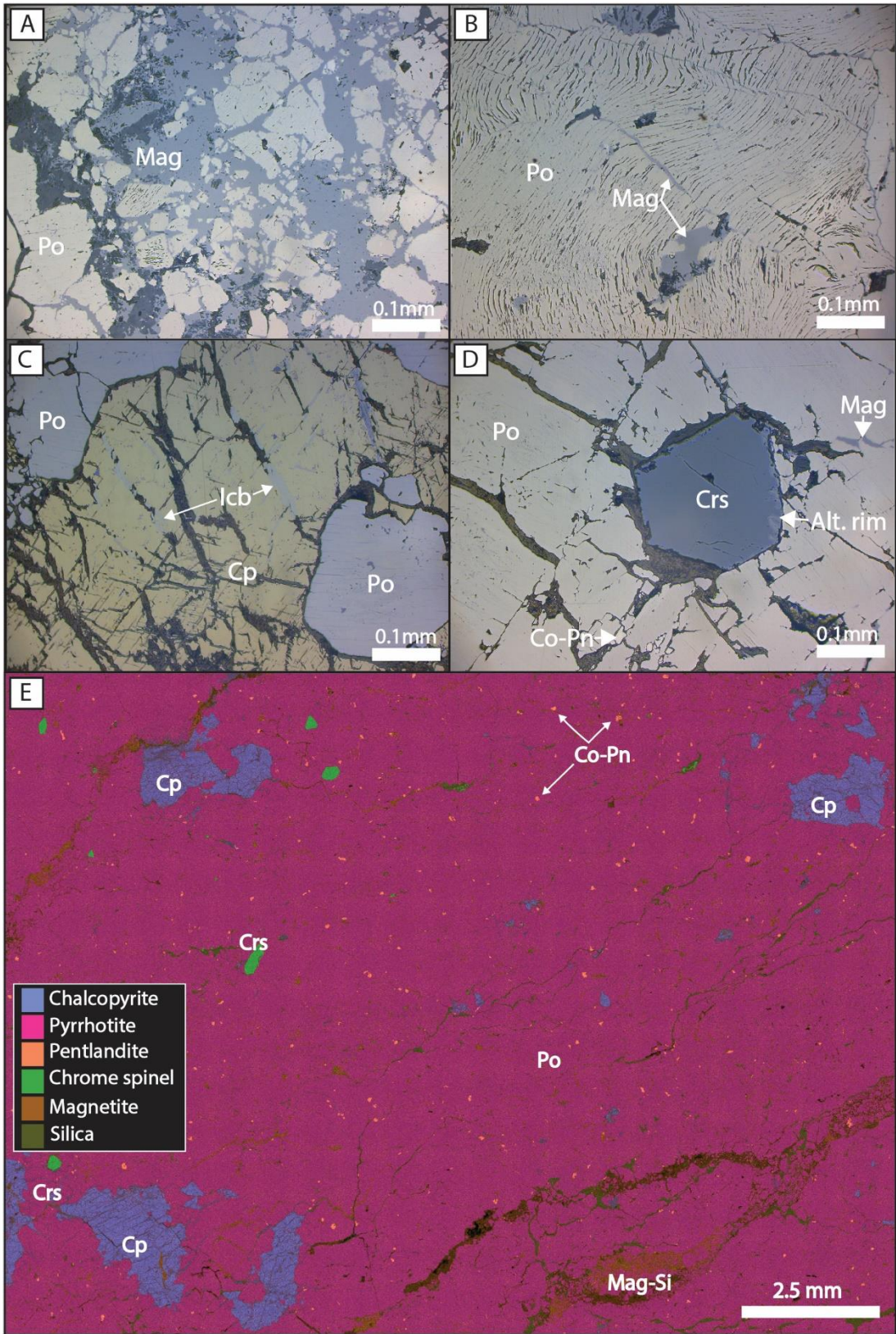
1098  
1099  
1100  
1101  
1102  
1103  
1104  
1105  
1106  
1107  
1108  
1109  
1110  
1111  
1112  
1113  
1114  
1115  
1116  
1117  
1118  
1119  
1120  
1121  
1122  
1123  
1124  
1125  
1126



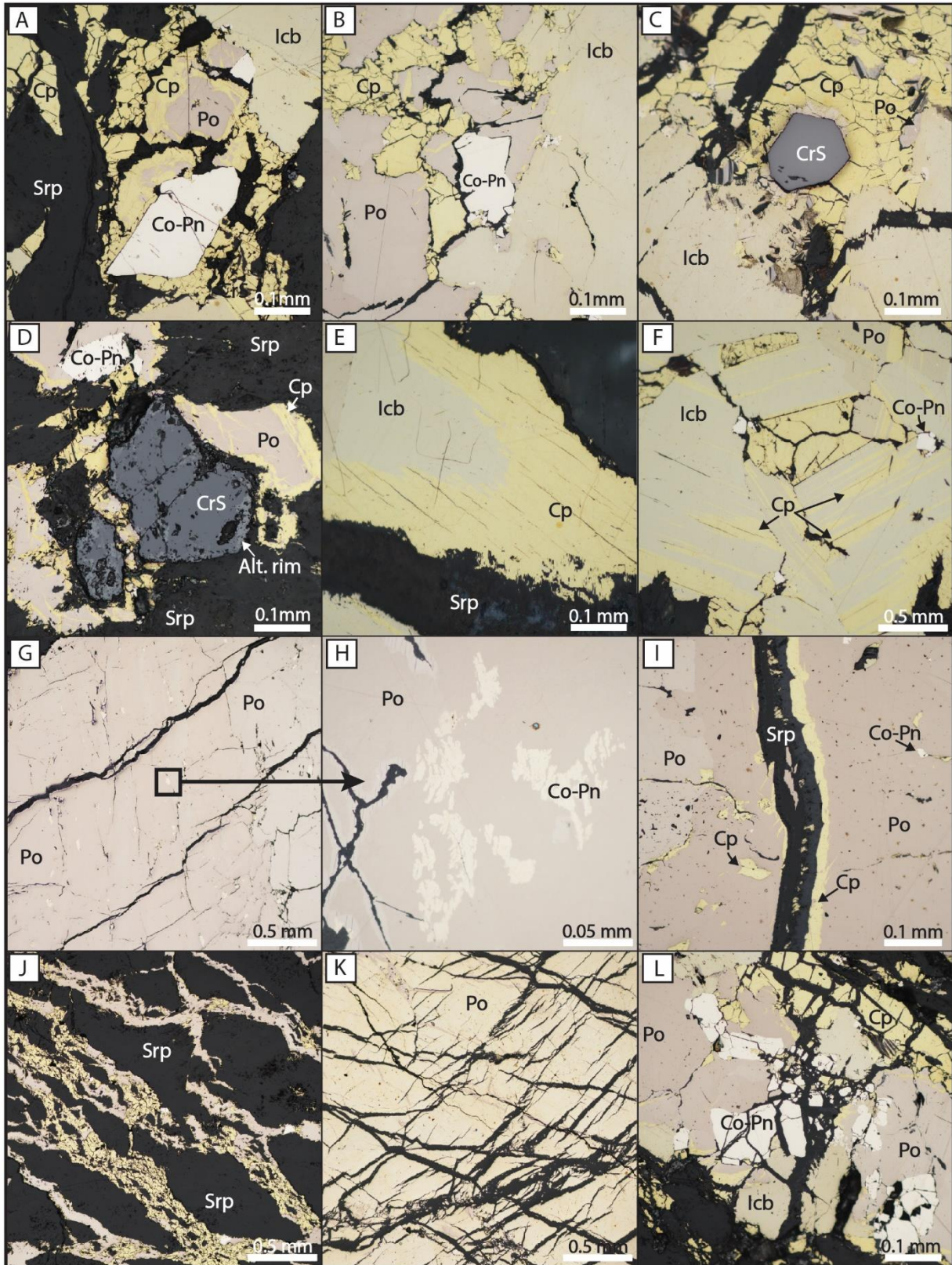


1127 Figure 3:

1128  
1129  
1130  
1131  
1132  
1133  
1134  
1135  
1136  
1137  
1138  
1139  
1140  
1141  
1142  
1143  
1144  
1145  
1146  
1147  
1148  
1149  
1150  
1151  
1152  
1153  
1154  
1155  
1156

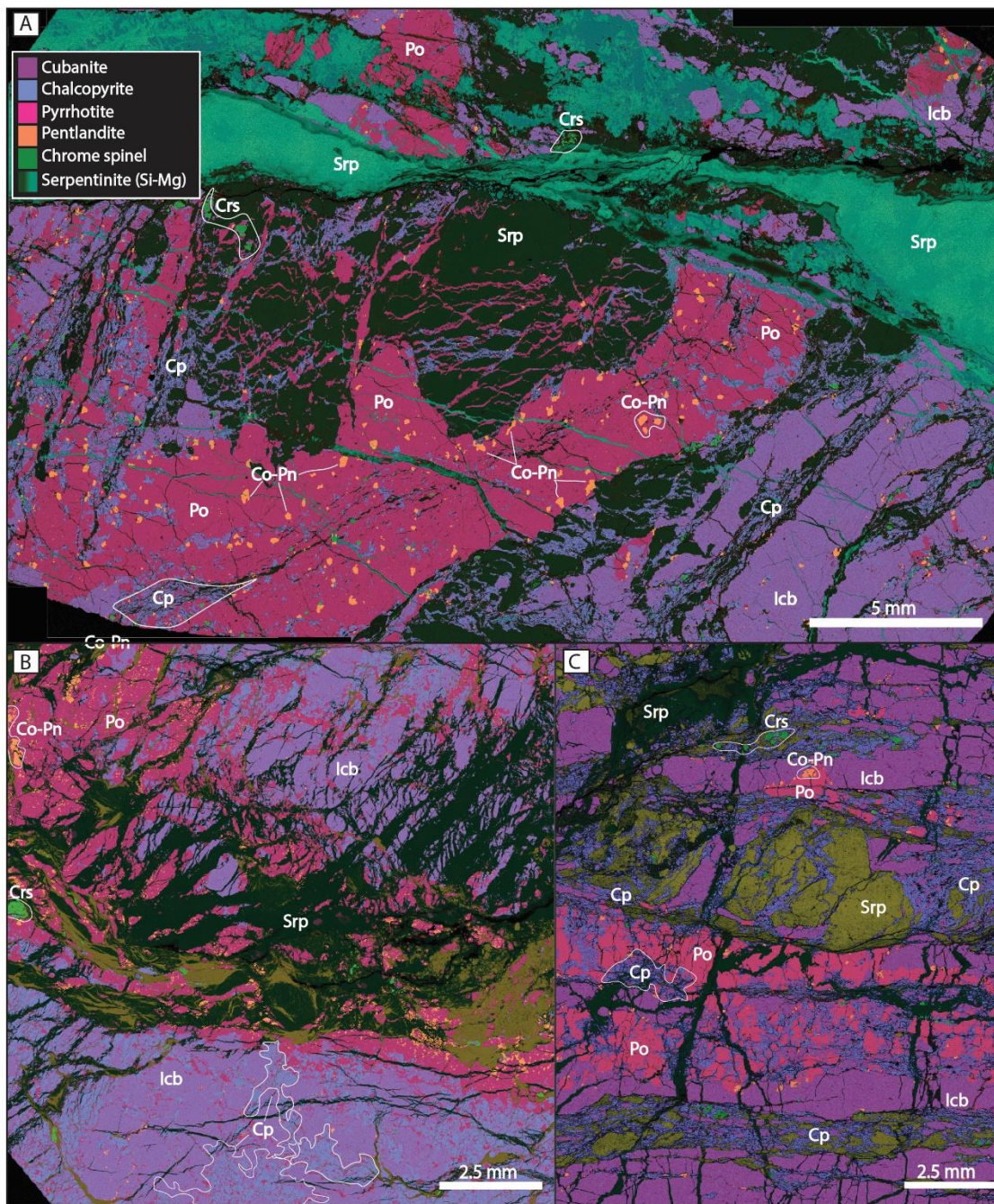


1157 Figure 4:



1158

1159 Figure 5:



1160

1161

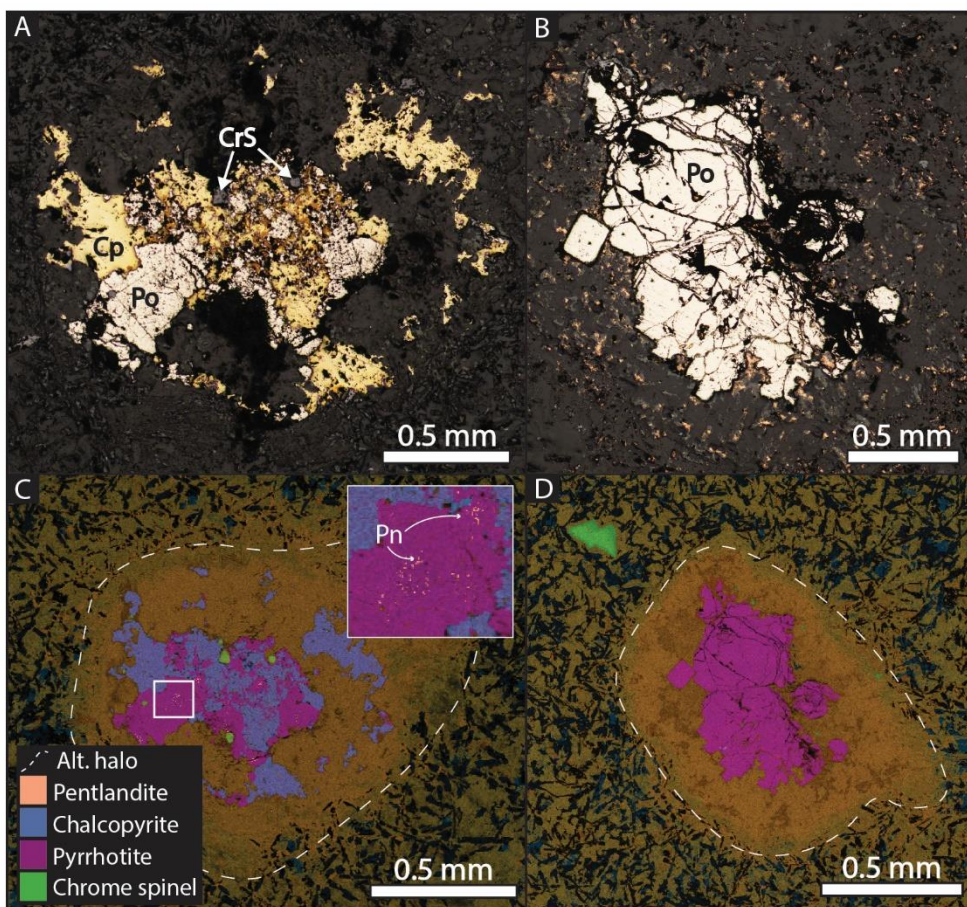
1162

1163

1164

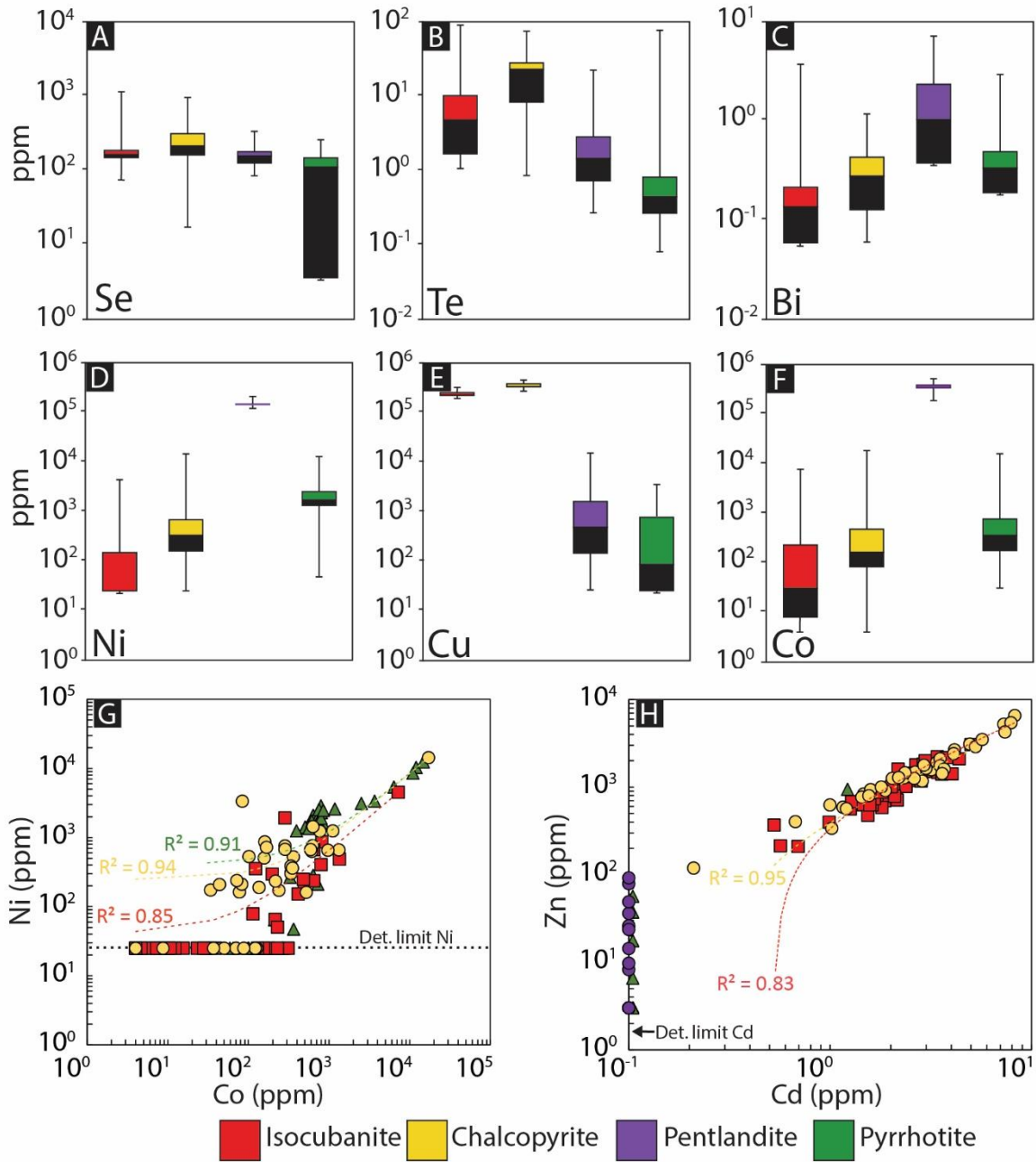
1165

1166 Figure 6:



1167  
1168  
1169  
1170  
1171  
1172  
1173  
1174  
1175  
1176  
1177  
1178  
1179

1180 Figure 7:



1181

1182

1183

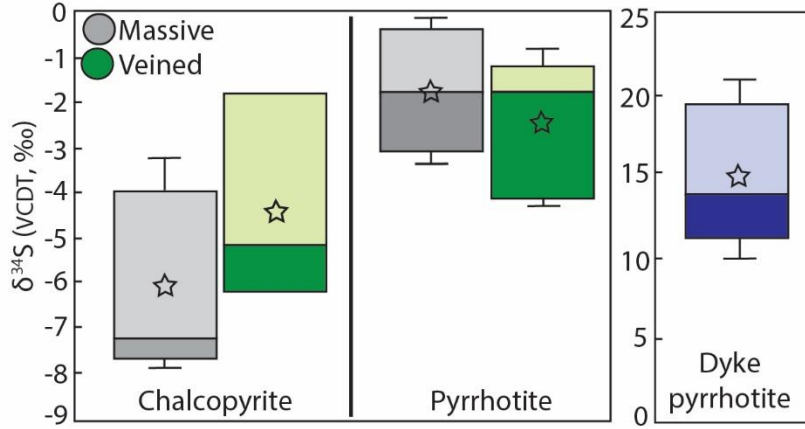
1184

1185

1186

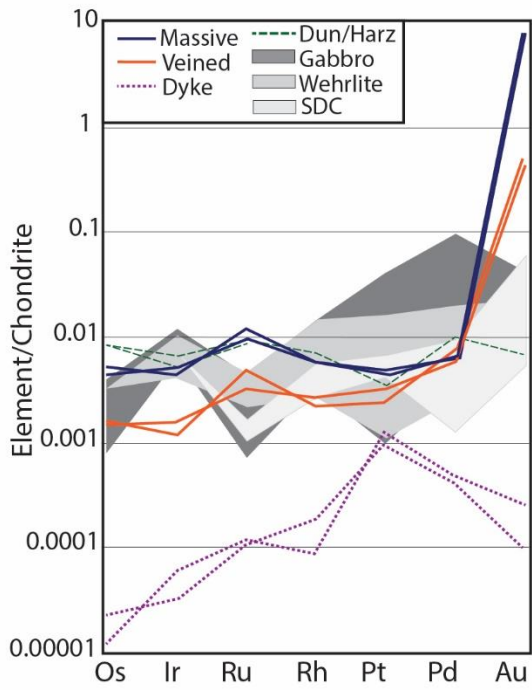
1187

1188 Figure 8:



1197

1198 Figure 9:



1199

1200

1201

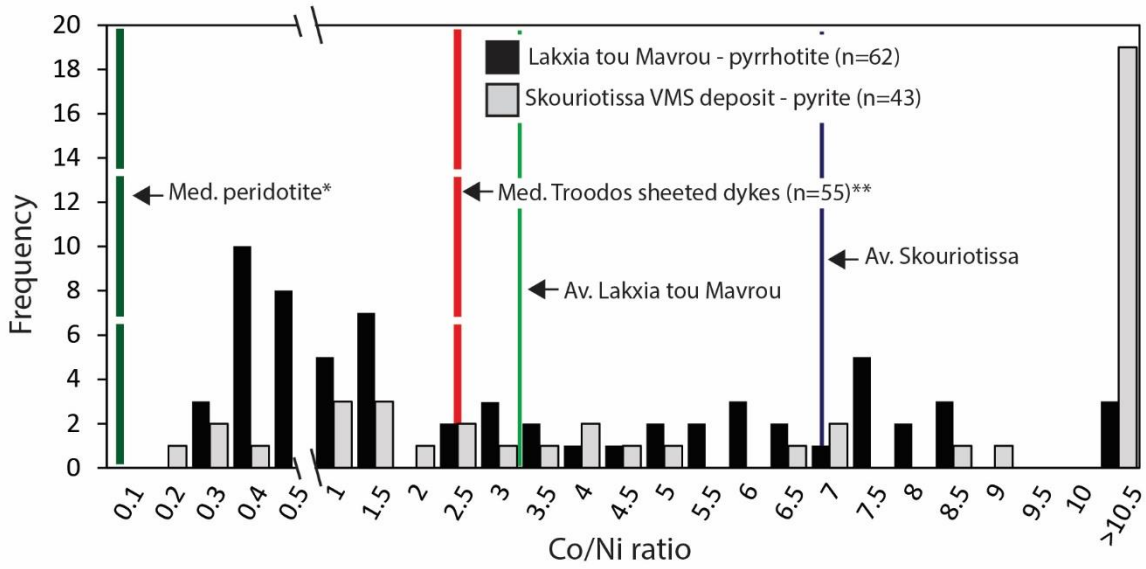
1202

1203

1204

1205

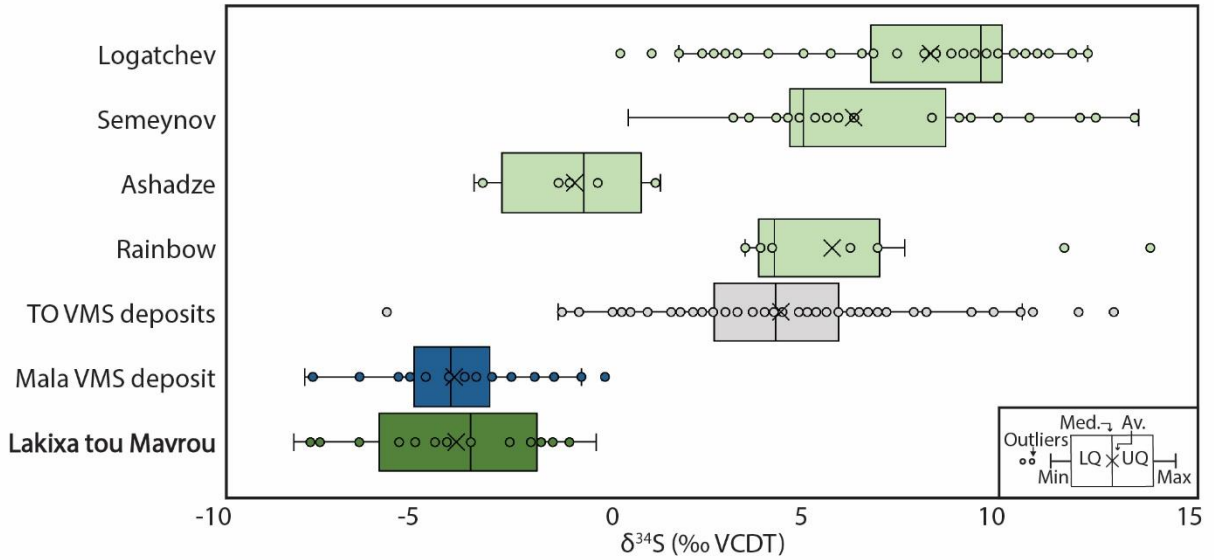
1206 Figure 10:



1207

1208

1209 Figure 11:



1210

1211

1212

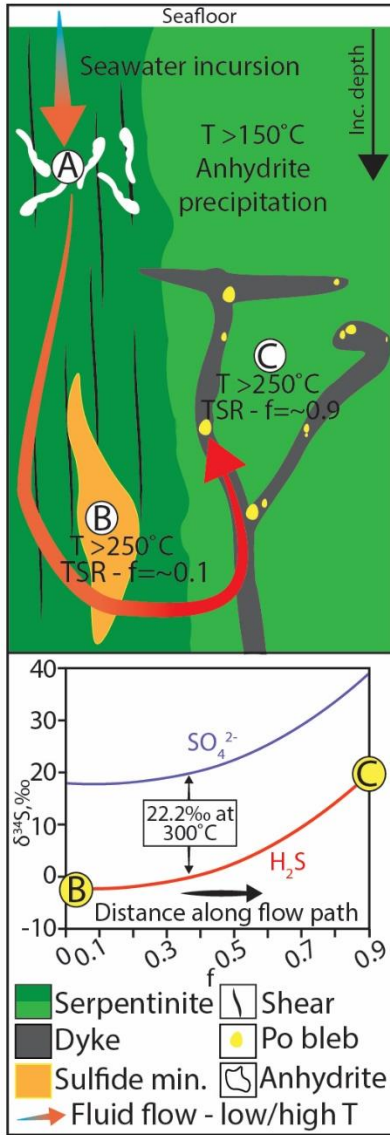
1213

1214

1215

1216

1217 Figure 12:



1218

1219

1220

1221

1222

1223

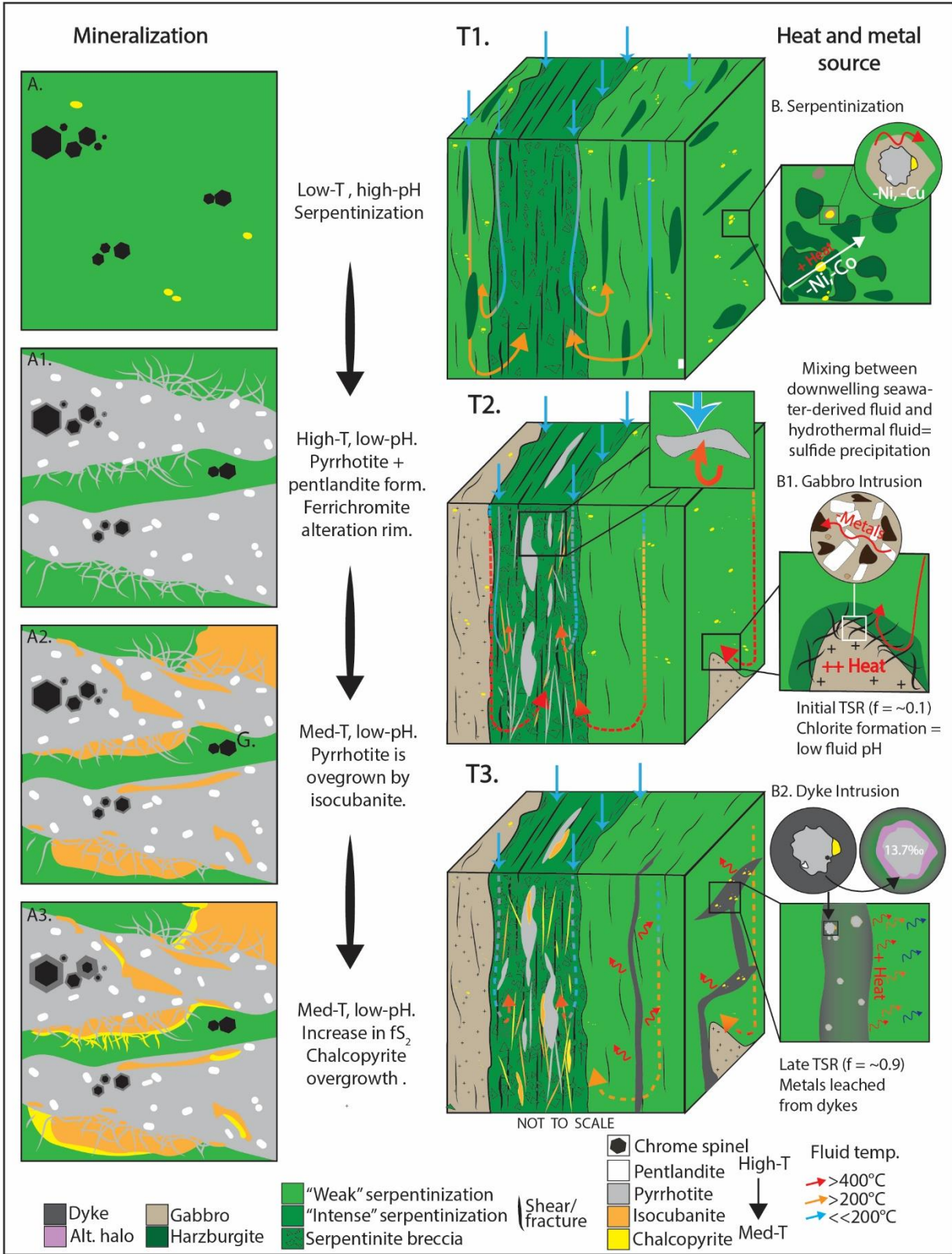
1224

1225

1226



1227 Figure 13:



1228

1229 Table 1:

	S/Se	Fe	Co	Ni	Cu	Zn	As	Se	Ag	Cd	Sb	Te	Au	Pb	Bi
		wt%	ppm	ppm	wt%	ppm	ppm	ppm	ppm	ppm	ppm	ppm	ppm	ppm	ppm
<b>Pyrrhotite</b>	<i>n=62</i>														
Med.	3420	60.6	349	1706	0.01	3.0	-	111	0.08	0.11	0.07	0.44	0.01	1.20	0.33
Av.	37668	60.7	1173	2461	0.05	19.8	-	91.1	0.36	0.12	0.08	1.86	0.06	1.65	0.46
1σ	48314	2.02	2781	2372	0.07	119	-	76.7	1.10	0.14	0.12	9.85	0.16	1.90	0.51
<b>Chalcopyrite</b>	<i>n=38</i>														
Med.	1645	33.1	163.5	329	35.3	1451	-	213	0.26	2.75	0.40	22.6	0.01	1.20	0.27
Av.	3558	33.4	745	856	34.8	1840	-	262	0.72	3.14	1.51	21.1	0.02	1.29	0.31
1σ	5077	1.48	2673	146209	1.59	1423	-	208	1.42	1.97	2.99	14.9	0.01	0.52	0.25
<b>Isocubanite</b>	<i>n=45</i>														
Med.	2120	43.6	29.5	25.0	25.0	875	-	165	1.26	2.02	0.07	4.70	0.01	1.20	0.13
Av.	2045	43.1	339	250	25.6	1074	-	234	1.39	2.23	0.23	10.6	0.01	1.51	0.23
1σ	749	2.31	1081	724	2.55	610	-	231	0.76	1.00	0.58	16.5	0.03	1.52	0.54
<b>Co-Pentlandite</b>	<i>n=34</i>														
Med.	2188	23.3	345095	150931	0.05	3.0	21.9	153.1	0.08	-	0.23	1.44	0.01	1.20	1.01
Av.	2272	23.9	330001	18897	0.19	12.8	21.9	162.3	0.24	-	0.69	3.45	0.09	1.20	1.66
1σ	681	2.96	59164	1.89	0.34	21.5	5.04	55.5	0.37	-	1.03	5.41	0.26	0.00	1.76
<b>Dyke pyrrhotite</b>	<i>n=6</i>														
Med.	3422	60.1	542.1	1706	0.003	3.00	0.55	111	0.08	0.11	0.07	0.43	0.01	1.20	0.35
Av.	40088	59.4	1363.4	2461	0.04	22.6	6.03	93.0	0.38	0.12	0.08	2.32	0.07	1.83	0.49
1σ	48299	7.80	2821.2	2809	0.06	121	19.9	82.4	1.12	0.14	0.13	10.1	0.16	2.01	0.52

1230

1231

1232 Table 2:

	Os	Ir	Ru	Rh	Pt	Pd	Au
	ppb	ppb	ppb	ppb	ppb	ppb	ppb
<b>Vein</b>	1.20	1.23	3.48	0.59	4.96	5.27	74.3
<b>Vein</b>	1.27	0.95	5.44	0.51	4.08	6.45	85.0
<b>Massive</b>	3.28	3.66	9.64	1.33	7.66	6.00	1090
<b>Massive</b>	3.75	3.23	12.1	1.28	6.98	5.77	1146
<b>Dyke</b>	0.02	0.03	0.14	0.05	1.65	0.43	0.03
<b>Dyke</b>	0.01	0.06	0.16	0.02	2.08	0.50	0.07

1233